A machine-learning reconstruction of sea surface pCO_2 in the North American Atlantic Coastal Ocean Margin from 1993 to 2021

Zelun Wu[1,2], Wenfang Lu[3*], Alizée Roobaert[4], Luping Song[5], Xiao-Hai Yan[2], and Wei-Jun Cai[2]

[1] State Key Laboratory of Marine Environmental Science & College of Ocean and Earth Science, Xiamen University, Xiamen, Fujian, China, 361102
[2] School of Marine Science and Policy, University of Delaware, Newark, Delaware, USA, 19716
[3] School of Marine Sciences, State Key Laboratory of Environmental Adaptability for Industrial Products, Sun Yat-sen University, Zhuhai, Guangdong, China, 519082
[4] Flanders Marine Institute (VLIZ), Jacobsenstraat 1, Ostend, Belgium, 8400
[5] School of Marine Science and Technology, Zhejiang Ocean University, Zhoushan, Zhejiang, China, 316022

Correspondence to: Wenfang Lu (luwf6@sysu.edu.cn)

Abstract. Insufficient spatiotemporal coverage of the partial pressure of CO_2 (pCO_2) observations has hindered precise carbon cycle studies in coastal oceans and justifies the development of spatially and temporally continuous pCO_2 data products. Earlier pCO_2 products have difficulties in capturing the heterogeneity of regional variations and decadal trends of pCO_2 in the North American Atlantic Coastal Ocean Margin (NAACOM). This study developed a regional reconstructed pCO_2 product for the NAACOM (Reconstructed Coastal Acidification Database-pCO_2, or ReCAD-NAACOM-pCO_2) using a two-step approach combining random forest regression and linear regression. The product provides monthly pCO_2 data at 0.25° spatial resolution from 1993 to 2021, enabling investigation of regional spatial differences, seasonal cycles, and decadal changes in pCO_2. The observation-based reconstruction was trained using Surface Ocean CO_2 Atlas (SOCAT) observations as observational values, with various satellite-derived and reanalysis environmental variables known to control sea surface pCO_2 as model inputs. The product shows high accuracy during the model training, validation, and independent test phases, demonstrating robustness and capability to accurately reconstruct pCO_2 in regions or periods lacking direct observational data. Compared with all the observation samples from SOCAT, the pCO_2 product yields a determination coefficient of 0.92, a root-mean-square error of 12.70 µatm, and an accumulative uncertainty of 23.25 µatm. The ReCAD-NAACOM-pCO_2 product demonstrates its capability to resolve seasonal cycles, regional-scale variations, and decadal trends of pCO_2 along the NAACOM. This new product provides reliable pCO_2 data for more precise studies of coastal carbon dynamics in the NAACOM region. The dataset is publicly accessible at https://doi.org/10.5281/zenodo.11500974 (Wu et al., 2024a) and will be updated regularly.

1 Introduction

Accurate and comprehensive sea surface partial pressure of CO_2 (pCO_2) datasets are necessary for quantifying coastal CO_2 uptake and assessing the impact of climate change on coastal ocean ecosystems. On a global scale, the coastal ocean, covering 8.4% (30.4×10^6 km^2) of the global ocean surface area (Chen et al., 2013; Dai et al., 2022), plays a significant role in the global carbon budget, accounting for approximately 10.9% of the global ocean CO_2 uptake from the atmosphere (0.25 of 2.3 Pg C yr^{-1}) on the global average (Dai et al., 2022; Friedlingstein et al., 2023). However, on regional scales, areal-based CO_2 uptake fluxes in specific coastal regions are often much greater than those in open oceans despite their less distinguishable global means (Dai et al., 2022). This is because sea surface pCO_2 is highly variable due to the influence of various physical and biogeochemical processes in coastal oceans, such as riverine input, upwelling, tidal mixing, and large-scale circulations (Laruelle et al., 2018; Roobaert et al., 2024b). Thus, accurately quantifying the CO_2 uptake in specific coastal regions becomes particularly challenging when only using observations due to the incomplete coverage of pCO_2 data in space and time.

This study focuses on the North American Atlantic Coastal Ocean Margin (NAACOM, **Fig. 1**). The entire region is defined as the area within 400 km of the coastline and divided into six sub-regions based on their geographic location following Fennel et al. (2019), including the Gulf of Mexico (GoMx), South Atlantic Bight (SAB), Mid-Atlantic Bight (MAB), Gulf of Maine (GoMe), Scotian Shelf (SS), and Gulf of St. Lawrence & Grand Banks (GStL&GB). The carbonate system in the NAACOM is influenced by large-scale circulations (**Fig. 1**), including the Gulf Stream and Labrador Current, as well as local processes like river discharge, export from marshes, and upwellings dynamics (Cai et al., 2020; Fennel et al., 2019; Wang et al., 2013). These complex physical and biogeochemical processes contribute to substantial spatial and temporal heterogeneity in sea surface pCO_2 across the NAACOM (Cai et al., 2020). Elucidating the driving mechanisms of these spatiotemporal pCO_2 variations necessitates extensive data coverage in time and space in this region. Over the past two decades, coastal field investigation efforts in this region have substantially increased through programs like the East Coast Ocean Acidification (ECOA) and Gulf of Mexico Ecosystems and Carbon Cruise (GOMECC) (Cai et al., 2020; Wang et al., 2013; Wanninkhof et al., 2015). Underway measurements from these cruises, combined with underway measurements from volunteer observing ships and buoys, are quality-controlled and compiled in the Surface Ocean CO_2 Atlas (SOCAT) database (Bakker et al., 2016), substantially advancing our understanding of coastal inorganic carbon chemistry along the NAACOM (Cai et al., 2020).

Despite significant progress in observational efforts, the spatial and temporal coverage of pCO_2 data remains limited in the NAACOM, with observations encompassing only 2.9 % of grid cells during the period 1993-2021 (**Fig. 2**). Observations are concentrated in the southern regions, with fewer samples available during winter. This data scarcity introduces substantial uncertainty in the air-sea CO_2 exchange quantification and hinders a comprehensive understanding of coastal inorganic carbon

dynamics, particularly in areas north of Cape Cod where measurements are highly sparse (**Fig. 2**). For example, reported air-sea CO_2 fluxes for the GoMe exhibit a wide range spanning from -0.50 to +2.50 mol C m^{-2} yr^{-1}, with conflicting reports characterizing it as a CO_2 source (Fennel & Wilkin, 2009; Vandemark et al., 2011), CO_2 neutral (Signorini et al., 2013), and 60 CO_2 sink (Cahill et al., 2016; Rutherford et al., 2021), underscoring the need for improved pCO_2 data coverage.
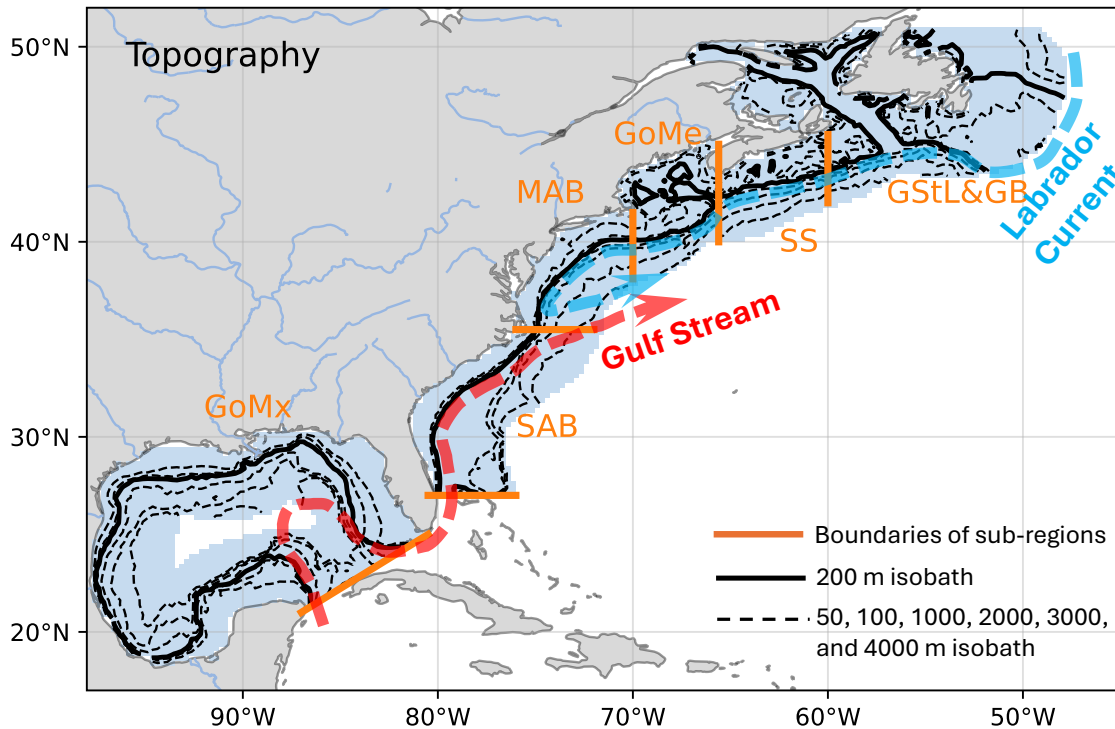

Figure 1. Topography (in meters) and large-scale circulation along the North American Atlantic Coastal Ocean Margin (NAACOM). The study region, defined as coastal areas extending 400 km offshore, is indicated by blue shading. The thick black line is the 200 m isobath, which roughly marks the shelf break and typically defines the continental shelf boundary. The 65 Gulf Stream (thick red dashed line with an arrow) flows northward along the east coast of the United States before veering eastward into the open Atlantic Ocean around Cape Hatteras. The Labrador Current (thick light blue dashed line with an arrow) flows southward along the east coast of Canada before meeting the Gulf Stream. Following Fennel et al. (2019), the study region is divided into six sub-regions by straight orange lines: the Gulf of Mexico (GoMx), South Atlantic Bight (SAB), Mid-Atlantic Bight (MAB), Gulf of Maine (GoMe), Scotian Shelf (SS), and Gulf of St. Lawrence and Grand Banks (GStL&GB). 70 Dashed contour lines indicate bathymetric depths of 50 m and 100 m on the shelf (from coastline to 200 m isobath), and 1000 m, 2000 m, 3000 m, and 4000 m from the shelf break to the open ocean.

3

Recently, various pCO_2 products, global or regional, with full coverage in time and space have been developed as essential supplements to observations. These products usually employed diverse algorithms and utilized environmental proxies from satellites and reanalysis products as model inputs and SOCAT observations as constraints to reconstruct the pCO_2 field with full temporal and spatial coverage. The development of those products has significantly advanced our understanding of inorganic carbon chemistry and the ocean carbon cycle. For example, seven global pCO_2 products were used to evaluate the ocean CO_2 uptake in the Global Carbon Budget 2023 edition (Friedlingstein et al., 2023). However, most of these products reconstruct pCO_2 in the open ocean, with coastal regions often being extrapolated or excluded. Currently, only one pCO_2 product has been developed specifically for the coastal ocean on a global scale (Laruelle et al., 2017; Roobaert et al., 2024a). This product was recently combined with an open ocean product to create a global reconstruction of the ocean CO_2 sink (Landschützer et al., 2020) and has since been utilized to narrow the variability in global reconstructions (Fay et al., 2021). However, global products primarily aim to ensure high accuracy of parameters on a global average; they may not guarantee equivalent accuracy for spatiotemporal variations on the regional scale. In comparison, regional pCO_2 products have demonstrated superior capability in resolving detailed small-scale variations.

Within the NAACOM region, several area-specific pCO_2 products have been reconstructed, focusing on specific regions such as the GoMx (e.g., Chen and Hu, 2019; Fu et al., 2020; Lohrenz and Cai, 2006) and the SAB and MAB (e.g., Wang et al., 2024; Xu et al., 2020). These regional and global pCO_2 products are valuable for validating model estimations (Roobaert et al., 2022; Ross et al., 2023). However, existing products often have limitations in spatial coverage, temporal resolution, or trend analysis capabilities. For instance, Chen and Hu (2019) provided a high-resolution (4 km) pCO_2 product for the GoMx, but this product faces challenges in capturing decadal changes in pCO_2 (Wu et al., 2024b). Conversely, Xu et al. (2020) successfully captured decadal trends of pCO_2, but only as area-averaged pCO_2 time series for the SAB and MAB, lacking comprehensive spatial coverage. Signorini et al. (2013) reconstructed a product using multiple linear regression (MLR) covering the areas from SAB to SS, but it spans only 8 years (2003-2010). Despite these valuable efforts, there remains a lack of comprehensive data products that adequately capture regional variations, seasonal cycles, and decadal changes in pCO_2 simultaneously for the entire NAACOM.

This study aims to develop a regional pCO_2 product specifically designed for the NAACOM, encompassing coastal regions extending 400 km offshore from the GoMx to the GB (**Fig. 1**). We integrated random forest and linear regression methods with hydrological parameters from satellite observations and reanalysis data to generate a monthly reconstructed pCO_2 product at 0.25° spatial resolution spanning the period from 1993 to 2021. The pCO_2 product, termed 'Reconstructed Coastal Acidification Database' or 'ReCAD-NAACOM-pCO_2', is specifically designed to resolve spatial variations, seasonal cycles, and decadal changes of pCO_2 along the NAACOM.

The structure of this paper is as follows: Section 2 details the methodology used to reconstruct ReCAD-NAACOM-pCO$_2$ and describes the datasets employed. Section 3 evaluates the accuracy of the reconstructed product, performance, and applicability in resolving seasonal cycles, regional variations, and decadal trends of pCO$_2$. Sections 4 and 5 provide links to access the dataset and codes used for generating the dataset and figures presented in this study. The final section summarizes the conclusions. ReCAD-NAACOM-pCO$_2$ demonstrates enhanced capability in resolving spatial variations and capturing the seasonal cycle and decadal trends of pCO$_2$ than the global products across different sub-regions along the NAACOM. This product offers improved insights into coastal carbon dynamics in this complex region, addressing the need for a comprehensive pCO$_2$ dataset in the NAACOM. Applications of this data product to examine the processes controlling the spatial variability, seasonal cycle, and decadal trends of pCO$_2$ and air-sea CO$_2$ flux will be published separately.

2 Data and methods

### 2.1 Observational data from SOCAT

The observational data for training the regression model were the seawater fugacity of CO$_2$ (fCO$_2$) measurement extracted from the SOCAT database (version 2023). fCO$_2$ represents the pCO$_2$ corrected for the non-ideal behavior of the gas in seawater, and both are commonly used in oceanographic studies. SOCAT compiles quality-controlled fCO$_2$ measurements from various platforms, including research vessels, commercial ships, and moorings (Bakker et al., 2016). This study used the monthly gridded SOCAT coastal product with a spatial resolution of 0.25° × 0.25° (but with data gaps). The gridded product incorporated measurements with quality flags A, B (uncertainty of 2 µatm), C, and D (uncertainty of 5 µatm) (Bakker et al., 2016). Over the period of 1993-2021, the SOCAT product encompassed 55,347 grid cells within our study area (**Fig. 2**), accounting for approximately 2.9% of the total grid cells in the NAACOM. Observational data show lower sampling density in the areas north of Cape Cod and western and southern GoMx (blue box in **Fig. 2**). The temporal distribution of samples exhibits a notable bias, with reduced collection during winter (**Fig. 2d**). Despite these spatial and temporal heterogeneities, the SOCAT observations provide coverage across all sub-regions and seasons of the NAACOM (**Fig. 2**). This comprehensive, albeit sparse, coverage facilitates the reconstruction of the fCO$_2$ and pCO$_2$ field through interpolation and regression techniques.

5
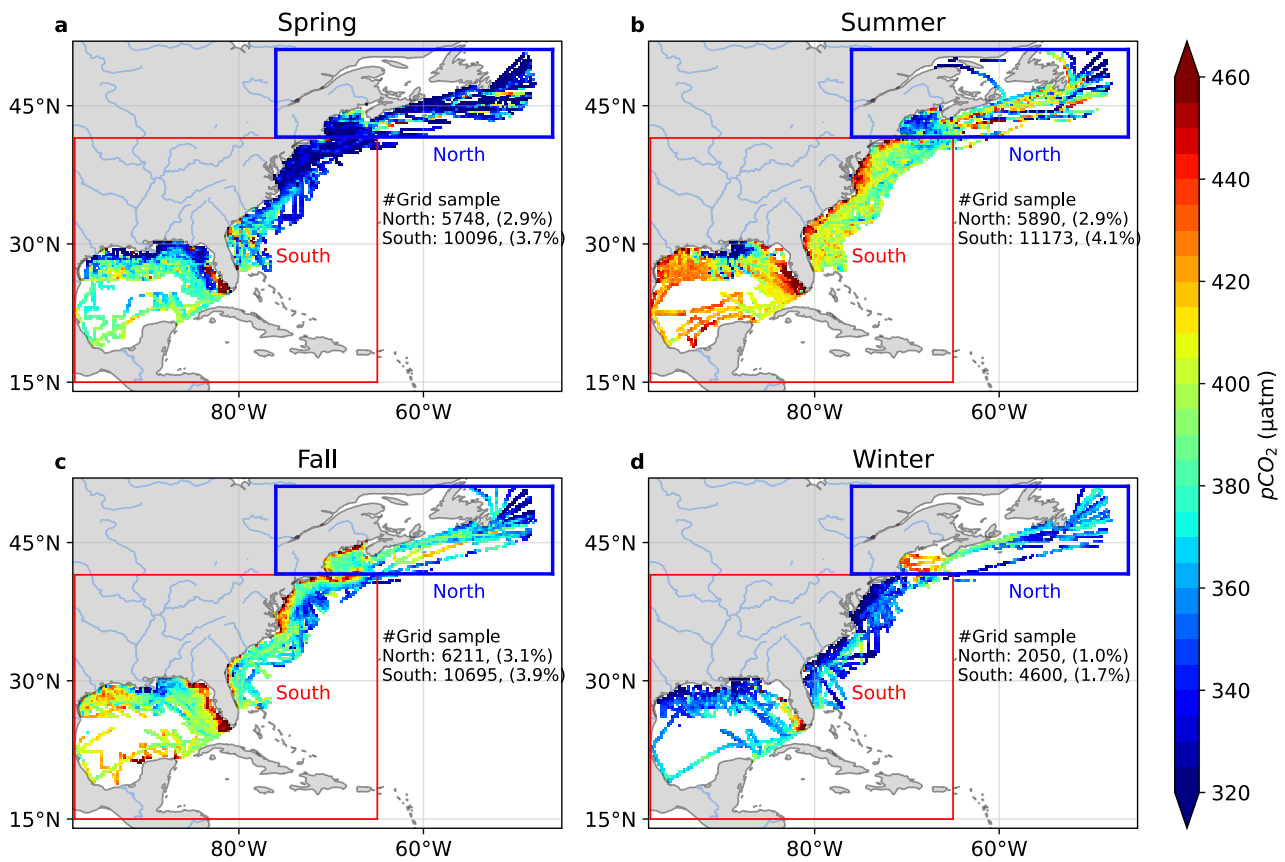
Figure 2. Spatial distribution of sea surface pCO_2 observations from SOCAT database (version 2023) in the NAACOM across four seasons from 1993 to 2021. Grid samples with data were counted by season: **(a)** Spring (March to May), **(b)** Summer (June to August), **(c)** Fall (September to November), and **(d)** Winter (December to February). The study region is divided into northern (blue box) and southern (red box) areas at approximately 41.5°N (Cape Cod). The number and percentage of grid samples are indicated for each region per season. Color scale represents pCO_2 values in μatm. Higher sampling density is evident in the southern area. Winter shows the lowest overall sampling coverage. Note that the SOCAT database provides quality-controlled fCO_2 measurements as the default parameter, which are subsequently converted to pCO_2 using Eq. (2).

2.2 Model design
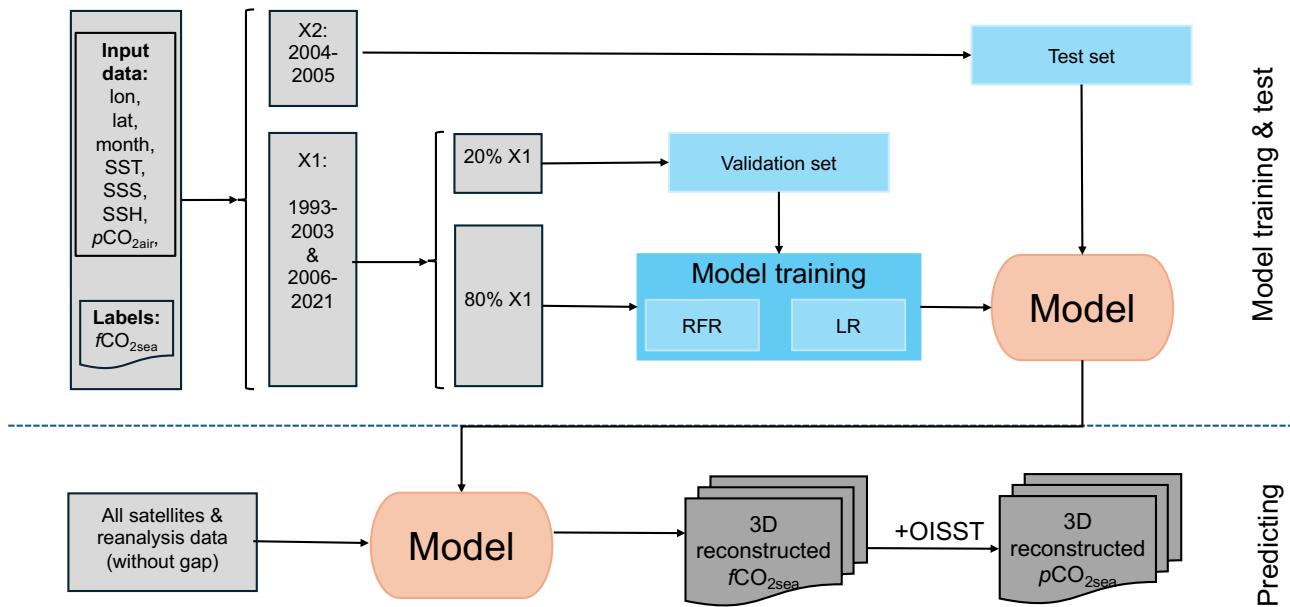
Figure 3. A flowchart of the two-step machine learning regression model for generating the reconstructed pCO_2 product. Grey boxes represent the input and output datasets, blue boxes illustrate the model training, validation testing, and independent test processes, and orange boxes represent the final trained model for predicting the reconstructed product. The two models in the orange boxes are identical. The training data, consisting of paired input variables (lon, lat, month, sea surface temperature (SST), sea surface salinity (SSS), sea surface height (SSH), and atmospheric pCO_2 (pCO_{2air}) and corresponding sea surface fCO_2 (fCO_{2sea}) labels), is divided into two sets: X1 (1993-2003 and 2006-2021) and X2 (2004-2005). X1 is further randomly divided into subsets for model training set (80%) and validation set (20%). The predictive model combines a random forest regression (RFR) and a linear regression (LR) algorithm. The trained and validated regression model is then applied to all satellite and reanalysis data (without gaps) to generate the 3D reconstructed fCO_{2sea} product, which was then converted to pCO_{2sea} with satellite SST data.

The procedures of developing and reconstructing the pCO_2 product are illustrated in **Fig. 3**. Initially, the input variables and sea surface fCO_2 data were matched to create a comprehensive dataset. To maintain consistency with the SOCAT database, which reports sea water CO_2 concentrations as fCO_2, we adopted fCO_2 as the model training label and first-step output variable in our model. During the model development phase, fCO_2 measurements served as training labels for the machine learning algorithm. The matched dataset was then divided into two sets: X1, encompassing the periods 1993-2003 and 2006-2021, and X2, covering 2004-2005. Set X1 was further randomly subdivided, with 80% allocated for model training and the remaining 20% for validation test. Set X2 served as an independent test set. The model training set (80% of X1) was used to develop a

two-step RFR+LR regression model. The RFR is designed to capture complex, nonlinear relationships between the input variables and the target variable (i.e., fCO_2), while the LR model is subsequently applied to mitigate potential systematic biases in RFR-derived fCO_2 values arising from spatiotemporal heterogeneities in the SOCAT observational dataset **(Fig. 2)**. RFR, an ensemble learning technique, combines multiple decision trees to produce more accurate and stable predictions (Breiman, 2001; Lu et al., 2019). Each decision tree in the RFR is trained on a randomly selected subset of the input data, with the final prediction derived from the average output of all trees. This approach mitigates overfitting and enhances the generalization performance of the model, making it particularly suitable for large datasets with complex, nonlinear variable relationships. The RFR model was trained using 10-fold cross-validation, with optimized hyperparameters including a minimum leaf size of 1, bagging method for ensemble aggregation, and 300 learning cycles after tuning. After RFR model training, an LR model was applied to the RFR-estimated fCO_2 (fCO_{2est}) output to make sure the RFR model is not systematically biased:

$$fCO_{2obs} = a \times fCO_{2est} + b + \varepsilon \qquad (1)$$

where fCO_{2obs} is the observed fCO_2 from SOCAT, a is the linear regression coefficient, b is the intercept, and ε is the residual that the linear model cannot resolve. This additional step was implemented to mitigate potential systematic bias in the RFR model that could arise from areas with higher sampling density, thereby ensuring a more balanced representation across the entire study region. The comparison between estimated pCO_2 before and after LR calibration is presented in **Appendix A.** The calibration was applied to each grid cell individually. To increase the data pool for linear regression, samples within a 5×5 grid window in space (i.e., $1.25° \times 1.25°$) were aggregated for LR model development. As the available measurements could not cover every grid cell and were insufficient to produce continuous spatial maps of the calibration coefficients (i.e., a and b in Eq. (1)), we employed a locally interpolated regression strategy similar to Carter et al. (2018). Mathematically, given the spatial and temporal continuity of fCO_{2est} and fCO_{2obs}, the coefficients a and b must also be continuous in space and time. Therefore, we linearly interpolated the coefficients a and b across the NAACOM. The interpolated coefficients were subsequently used to adjust the RFR-derived fCO_{2est}.

The validation set, comprising 20% of X1 randomly sampled from 1993-2003 and 2006-2021, serves as a critical monitoring step for model evaluation. This subset plays two key roles: first, it tests hyperparameter tuning by providing independent performance metrics on unseen data, and second, it helps detect potential overfitting by monitoring the divergence between training and validation performance. While the validation set itself cannot prevent overfitting, it enables the detection of overfitting patterns when the performance of the model improves on training data but deteriorates on validation data. Through this continuous evaluation process, the validation set ensures more robust model development and helps achieving better generalization capabilities.

The independent test set (X2), covering the years 2004-2005, serves as a critical evaluation period specifically designed to assess the reliability of the model in predicting values for years that were completely excluded from both training and validation phases. Because we intentionally withhold these two years from model development, this approach directly tests the capability of the model to generate reliable predictions and fill temporal data gaps for periods without observational data.

Finally, the trained model is applied to all satellite and reanalysis data to generate the final gap-free reconstructed fCO_2 data. As most products reported seawater CO_2 concentration as pCO_2, we subsequently converted the reconstructed fCO_2 values to pCO_2 using the following equation (Takahashi et al., 2019) and our final product reports fCO_2 and pCO_2 both:

$$pCO_2 = fCO_2 \times (1.00436 - 4.669 \times 10^{-5} \times SST) \tag{2}$$

2.3 Regression model input variables from satellite and reanalysis

The input variables for training the regression model include longitude (lon), latitude (lat), month, sea surface temperature (SST), sea surface salinity (SSS), sea surface height (SSH), and atmospheric pCO_2 (pCO_{2air}). Longitude, latitude, and month serve as spatiotemporal predictors, enabling the algorithm to identify and capture regional and seasonal variability in fCO_2 within the study area (Su et al., 2020; Yang et al., 2024). SST, SSS, and SSH are critical variables that characterize the physical and biogeochemical ocean settings, which play a crucial role in determining the spatial and temporal variability of fCO_2. The pCO_{2air} represents the atmospheric forcing on the air-sea CO_2 exchange. Including pCO_{2air} is essential for accurately assessing the decadal pCO_2 trend.

SST data were obtained from the National Oceanic and Atmospheric Administration (NOAA) Optimum Interpolation Sea Surface Temperature (OISST) v2.1 product (Huang et al., 2021). The OISST dataset is a global gridded SST analysis that blends observations from various sources, including satellites, ships, and buoys. The dataset employs an optimum interpolation technique to combine these observations and generate a daily SST field at a spatial resolution of 0.25° × 0.25°. For this study, the daily SST data were averaged to create a monthly product.

SSS data were obtained from the Simple Ocean Data Assimilation (SODA) v3.15.2 product (Carton et al., 2018). SODA is a comprehensive reanalysis dataset that integrates a global ocean model with observational data to estimate ocean state variables consistently. The SODA system assimilates observations from multiple sources, including floats, moorings, and ship-based measurements, thereby constraining the model output and enhancing the accuracy of represented ocean physical properties, including SSS. The SODA v3.15.2 product offers monthly SSS data with a temporal resolution of one month and a spatial resolution of 0.5° × 0.5°, which were linearly interpolated to a 0.25° × 0.25° grid resolution to maintain consistency with other

input variables and the gridded SOCAT fCO$_2$ data. Noted that such interpolation could potentially introduce additional errors. We doubled the SSS uncertainty in the region, assuming this would encompass its true uncertainty (see **Appendix B**).

SSH data were extracted from the Global Ocean Gridded L4 Sea Surface Heights (European Union-Copernicus Marine Service, 2021) created by the Copernicus Marine Environment Monitoring Service (CMEMS). This product provides daily SSH data derived from altimeters, with a spatial resolution of 0.25° × 0.25° since 1993 (ongoing). Daily SSH data were averaged to monthly means.

pCO$_{2air}$ data converted from the mole fraction of CO$_2$ in the dry air (xCO$_{2air}$) were downloaded from the NOAA Marine Boundary Layer (MBL) reference product (Dlugokencky and Tans, 2022). The MBL reference provides weekly zonal average xCO$_{2air}$ measurements from a global observation network. The xCO$_{2air}$ data was linearly interpolated to the same spatial and temporal resolution as the other input variables (0.25° × 0.25°, monthly). xCO$_{2air}$ was converted to pCO$_{2air}$ with the equation:

$$pCO_{2air} = xCO_{2air} \times (P - p_w) \tag{3}$$

where P is the total atmospheric pressure on the sea surface, which was downloaded from the fifth generation European Centre for Medium-Range Weather Forecasts (ECMWF) reanalysis (ERA5) (Hersbach et al., 2019), and p_w is the water vapor pressure, which was calculated using the formula of Weiss & Price (1980) using SST from OISST and SSS from SODA.

2.4 Evaluation of model

The accuracy of the model outputs was assessed using several statistical metrics, including the coefficient of determination (R^2), root mean square error (RMSE), mean absolute error (MAE), and mean bias error (MBE). These metrics were calculated for the training and validation set phases, as well as for the independent validation set:

$$R^2 = 1 - \sum_i^N \left(y_{obs,i} - y_{est,i}\right)^2 / \sum_i^N \left(y_{obs,i} - \overline{y_{obs}}\right)^2 \tag{4}$$

$$RMSE = \sqrt{\frac{1}{N} \sum_i^N \left(y_{obs,i} - y_{est,i}\right)^2} \tag{5}$$

$$MAE = \frac{1}{N} \sum_i^N \left|y_{obs,i} - y_{est,i}\right| \tag{6}$$

$$MBE = \frac{1}{N} \sum_i^N \left(y_{obs,i} - y_{est,i}\right) \tag{7}$$

where i denotes the i-th sample, y_{obs} and $\overline{y_{obs}}$ are the observed pCO_2 values from SOCAT and their average, y_{est} represents the predicted pCO_2 values from the final model, and N is the total number of matched samples.

2.5 Uncertainty of reconstructed pCO_2

The uncertainty of estimated pCO_2 in our product for each grid cell was accumulated from four sources of uncertainties: the direct pCO_2 measurement uncertainty from SOCAT (u_{obs}), gridding uncertainty (u_{grid}), mapping uncertainty (u_{map}), and the uncertainty accumulated from the input variables (u_{inputs}). The first three sources of uncertainty were calculated according to the approach used by earlier reconstructed pCO_2 products (Landschützer et al., 2014; Roobaert et al., 2024a; Sharp et al., 2022). u_{obs} is inherited from the SOCAT observations. The SOCAT database uses discrete samples with quality flags A and B (accuracy < 2 µatm), and C and D (accuracy < 5 µatm) to create the gridded file. Adopting a conservative approach, we used the maximum u_{obs} of 5 µatm. u_{grid} was calculated as the standard deviation of the samples used to calculate the gridded fCO_2 in each grid cell. u_{map} is introduced by reconstructing the pCO_2 using the RFR-LR model. It was evaluated as the RMSE between the reconstructed pCO_2 and the observed pCO_2 values following Roobaert et al. (2024a) and Sharp et al. (2022). Given that the derivation of u_{obs}, u_{grid}, and u_{map} is contingent upon SOCAT observations, these three uncertainties and the total uncertainty u_{pCO_2} is reported on a sub-regional basis.

In addition to these three sources of uncertainty, this study incorporated cumulative uncertainties from input variables (u_{inputs}), including SST, SSS, SSH, and pCO_{2air}. These satellite-derived or reanalysis-based variables inherently possess uncertainties that propagate nonlinearly through the regression model, ultimately affecting the estimated pCO_2 values (Wang et al., 2021, 2023). We employed a Monte Carlo simulation to calculate u_{inputs}. For each input variable (SST, SSS, SSH, pCO_{2air}), we added white noise following a normal distribution $N(0, u_{x_i})$, where u_{x_i} is the uncertainty of the respective input variable x_i. We then recalculated pCO_2 using these noise-added inputs and determined the resulting changes in pCO_2. This process was repeated 100 times for each input variable, and the resulting uncertainty in pCO_2 from each variable was calculated as the standard deviation of the differences between the original reconstructed pCO_2 and the pCO_2 values after adding noise in each grid cell. The final u_{inputs} was computed as the square root of the quadratic sum of these individual uncertainties from the four input variables. Detailed procedures for determining u_{inputs} are described in **Appendix B.**

Assuming these sources are independent, the uncertainty of the estimated gridded pCO_2 in our product, u_{pCO_2}, was calculated using the error propagation (Hughes and Hase, 2010; Taylor, 1997):

$$u_{pCO_2} = \sqrt{u_{obs}^2 + u_{grid}^2 + u_{map}^2 + u_{inputs}^2} \tag{8}$$

11

2.6 Comparison with global reconstructed pCO_2 product

The ReCAD-NAACOM-pCO_2 product was evaluated through comparisons with seven reconstructed pCO_2 products that are developed for the global ocean and used in the Global Carbon Budget 2023 edition (Friedlingstein et al., 2023) and one reconstructed pCO_2 product that is specifically developed for the global coastal ocean (ULB_SOMFNN_coastal_v2, Roobaert et al., 2024a). Those data products reconstructed pCO_{2sea} data using different machine-learning algorithms. Detailed information on those products is summarized in **Table 1.**

Table 1. References for global pCO_2 products used to compare with ReCAD-NAACOM-pCO_2 in this study. The abbreviations in the Methods column are: RFRE for random forest-based Regression Ensemble, SOM-FFN for Self-Organizing Map-Feed Forward Network, MLR for Multiple Linear regression, FFNN for Feed-Forward Neural Network, XGB for eXtreme Gradient Boosting algorithm, and GRaCER for Geospatial Random Cluster Ensemble Regression.

| Data		Methods	Period	Resolution	Source
Open ocean product	MPI_SOM-FFN_v2022	SOM-FNN	1982-2021	1°×1°, monthly	Landschützer et al. (2017)
	Jena-MLS	MLR	1951-2021	2°×2°, monthly	Rödenbeck et al. (2022)
	CMEMS-LSCE-FFNNv2	Ensemble of nonlinear models	1985-2021	1°×1°, monthly	Chau et al. (2022)
	LDEO-HPD	XGB	1985-2018	1°×1°, monthly	Gloege et al. (2022)
	NIES-NN	FFNN	1980-2020	1°×1°, monthly	Zeng et al. (2014)
	JMA-MLR	MLR	1998-2022	1°×1°, monthly	Iida et al. (2021)
	OS-ETHZ-GRaCER	GRaCER	1982-2020	1°×1°, monthly	Gregor & Gruber (2021)
Coastal ocean product	ULB–SOM–FFN–coastalv2	SOM-FNN	1982-2020	0.25°×0.25°, monthly	Roobaert et al. (2024a)

3 Results and discussion

3.1 Evaluating the regression model performance

Our product employs a two-step RFR+LR algorithm to retrieve pCO_2. The initial RFR step accurately captures most seasonal and decadal pCO_2 variations across all six sub-regions (**Appendix A**). When comparing only at matching grid cells where SOCAT measurements are available, the differences ($N = 12$) in monthly mean climatology between SOCAT and RFR-derived pCO_2 are less than 2 µatm on average with standard deviations below 5 µatm across all sub-regions (**Fig. A1**). However, the RFR-derived pCO_2 shows lower accuracy in capturing long-term pCO_2 changes in the GoMe and SAB. The subsequent LR calibration improves the performance significantly: R^2 values increase from 0.69 to 0.81 in the GoMe and from 0.83 to 0.93 in the SAB, while RMSE decreases from 12.43 to 10.51 µatm in the GoMe and from 10.83 to 8.12 µatm in the SAB (**Fig. A2**).

The ReCAD-NAACOM-pCO_2 product demonstrated robust performance and high accuracy in capturing pCO_2 variability across the NAACOM (**Fig. 4**). During the model training phase, the product achieved an R^2 of 0.96, an RMSE of 9.1 µatm, an

MAE of 5.92 µatm, and an MBE of 0.05 µatm (**Fig. 4a**). The model demonstrated comparable performance metrics during the validation phase (**Fig. 4b**). To further evaluate generalizability and robustness of the model, we also conducted an independent test using data from 2004 to 2005, in which all data samples were not included in the model training and validation sets. During this independent test phase, the pCO_2 product maintained high accuracy, with $R^2 = 0.64$, RMSE = 27.2 µatm, MAE = 18.86 µatm, and MBE = 0.07 µatm **(Fig. 4c)**. Additionally, most independent validation samples were distributed around the 1:1 corresponding line, proving ability of the models in predicting pCO_2 across unsampled spatial and temporal domains without overfitting. The model consistently demonstrated strong performance during the training, validation, and independent test phases across all sub-regions **(Table 2)**. Overall, compared with all available samples in SOCAT, it achieved an R^2 of 0.92, an RMSE of 12.70 µatm, an MAE of 7.55 µatm, and an MBE of 0.13 µatm for the entire NAACOM **(Table 2)**, highlighting the generalizability of the ReCAD-NAACOM-pCO_2 product, and robustness in effectively capturing the variability in pCO_2 and providing reliable predictions of pCO_2 across the studied regions.
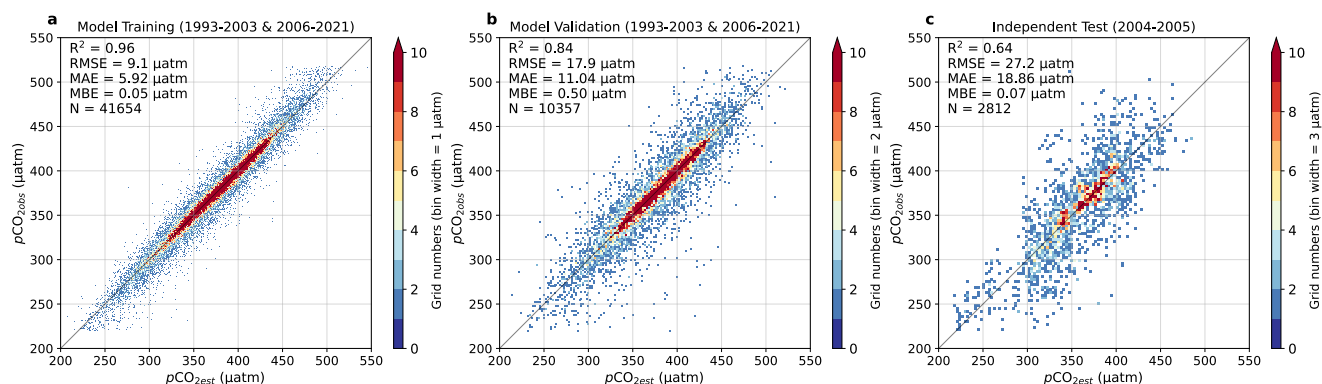
Figure 4. Evaluation of regression model for reconstructing ReCAD-NAACOM-pCO_2 product. Density scatter plots compare the product estimated pCO_2 (pCO_{2est}) with the in situ SOCAT observations (pCO_{2obs}) during the **(a)** model training phase (80% samples during the period of 1993-2003 and 2006-2021), **(b)** validation phase (20% samples during the period of 1993-2003 and 2006-2021), and **(c)** independent test phase (samples during the period of 2004-2005). Statistical metrics include the coefficient of determination (R^2), root mean square error (RMSE), mean absolute error (MAE), mean bias error (MBE), and the number of samples (N). The color bar represents the number of data points within each bin.

Table 2. Performance of the regression model during the model training, validation, and independent test phases across different sub-regions. The metrics include the coefficient of determination (R^2), root mean square error (RMSE), mean absolute error (MAE), and mean bias error (MBE). Sub-regions are the Gulf of Mexico (GoMx), South Atlantic Bight (SAB), Mid-Atlantic Bight (MAB), Gulf of Maine (GoMe), Scotian Shelf (SS), and Gulf of St. Lawrence and Grand Banks (GStL&GB).

Region	Type	R^2	RMSE (µatm)	MAE (µatm)	MBE (µatm)
GStL&GB	Training set	0.97	7.81	5.31	0.33
	Validation set	0.91	13.57	8.83	0.44
	Independent test set	0.76	25.23	16.82	-5.64
	All	**0.94**	**11.48**	**6.92**	**-0.15**
SS	Training set	0.96	9.35	6.61	-1.13
	Validation set	0.90	13.27	9.41	-0.90
	Independent test set	0.50	30.92	24.12	-3.50
	All	**0.90**	**13.82**	**8.89**	**-1.32**
GoMe	Training set	0.95	10.62	7.72	0.14
	Validation set	0.81	20.12	14.35	0.83
	Independent test set	0.49	31.66	23.95	3.72
	All	**0.90**	**14.91**	**9.97**	**0.49**
MAB	Training set	0.97	9.39	6.60	-0.06
	Validation set	0.84	19.49	13.47	-0.19
	Independent test set	0.56	37.93	28.53	7.13
	All	**0.93**	**13.26**	**8.44**	**0.08**
SAB	Training set	0.96	6.76	4.24	0.30
	Validation set	0.87	12.03	6.98	0.98
	Independent test set	0.73	23.60	16.75	1.33
	All	**0.91**	**10.63**	**5.95**	**0.52**
GoMx	Training set	0.94	9.13	5.14	0.08
	Validation set	0.76	19.08	9.82	0.74
	Independent test set	0.46	14.70	7.64	-4.49
	All	**0.90**	**11.86**	**6.10**	**0.09**
NAACOM	Training set	0.96	9.11	5.92	0.05
	Validation set	0.84	17.89	11.04	0.50
	Independent test set	0.64	27.17	18.86	0.07
	All	**0.92**	**12.70**	**7.55**	**0.13**

14

3.2 Spatial distribution of product bias

The ReCAD-NAACOM-pCO$_2$ product exhibited a negligible area-mean bias of +0.13 µatm with a standard deviation of 12.70 µatm when compared to all SOCAT observation grid cells across the entire NAACOM (**Fig. 5 and Table 2**). This small average difference suggests no consistent over- or under-estimation by the regression model, indicating reliability of the product in estimating the monthly and annual mean climatology of pCO$_2$ across the entire NAACOM region.
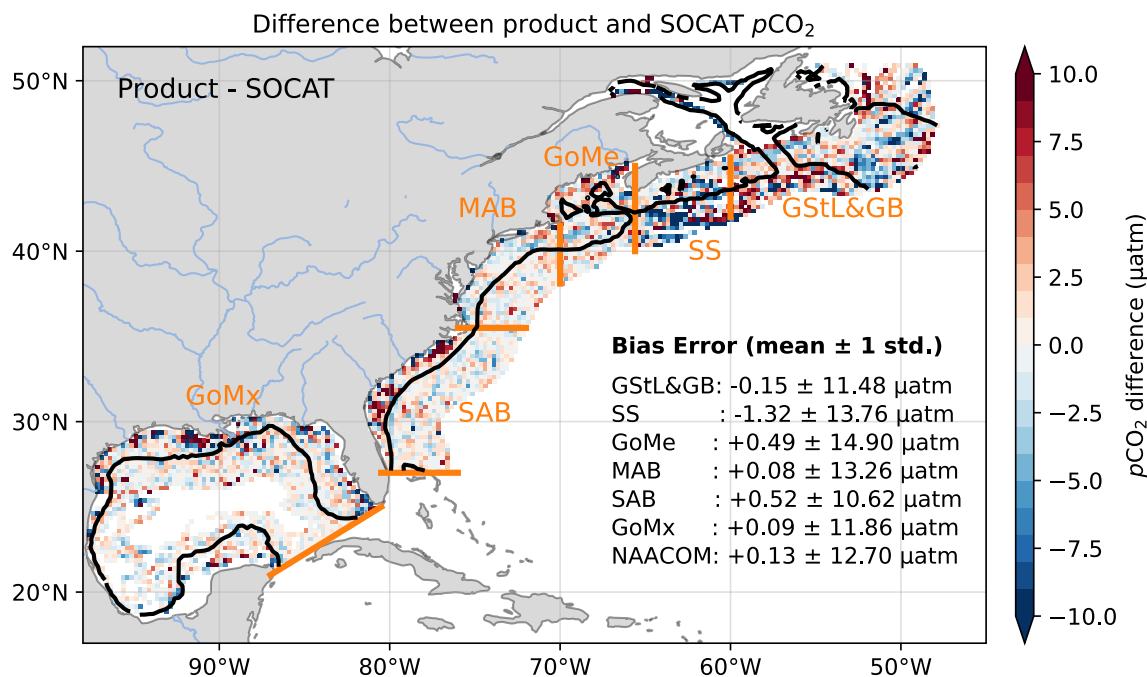

Figure 5. Spatial distribution of mean bias error (MBE) between ReCAD-NAACOM-pCO$_2$ product and SOCAT observations across the NAACOM. The MBE is calculated for each grid cell as the average difference between product estimates and SOCAT observations. Positive values (red) indicate product overestimation, while negative values (blue) indicate underestimation relative to SOCAT. Regional MBE values with one standard deviation are shown for each sub-region, corresponding to the values in the last column of Table 2. The overall bias error for the NAACOM is +0.13 ± 12.97 µatm. Following Fennel et al. (2019), the study region is divided into six sub-regions by straight orange lines: the Gulf of Mexico (GoMx), South Atlantic Bight (SAB), Mid-Atlantic Bight (MAB), Gulf of Maine (GoMe), Scotian Shelf (SS), and Gulf of St. Lawrence and Grand Banks (GStL&GB). The thick black line is the 200 m isobath, which roughly marks the shelf break and typically defines the continental shelf boundary.

While the area-average difference is small, the differences are distributed heterogeneously in space. Larger differences (absolute difference > 10 µatm) tend to occur in nearshore regions, particularly along the coastlines of the GoMx and SAB, as well as in northern areas such as the GoMe, SS, and GStL&GB (**Fig. 5**). These regional variations can be attributed to complex coastal processes such as terrestrial inputs, sparse observations in the northern areas (Lavoie et al., 2021; Rutherford et al., 2021; Salisbury and Jönsson, 2018), and less accurate satellite observations in the nearshore regions (Song et al., 2023). Conversely, smaller differences (absolute difference < 2.5 µatm) are observed in the central parts of the GoMx, offshore regions of the SAB and MAB, and some nearshore regions of the SS and GB, which is likely due to more stable oceanic conditions in those regions. Regional MBE for different machine learning development phases (training, validation, and test sets) are detailed in **Table 2**. Despite these regional differences, MBE of both the validation set (-1.0 ~ 1.0 µatm) and independent test set (-4.5 ~ 7.5 µatm) demonstrate minimal values across sub-regions (**Table 2**), underscoring the effectiveness of the product in capturing the broader pCO$_2$ patterns across the NAACOM.

3.3 Evaluating the capacity of the product in capturing pCO$_2$ seasonality
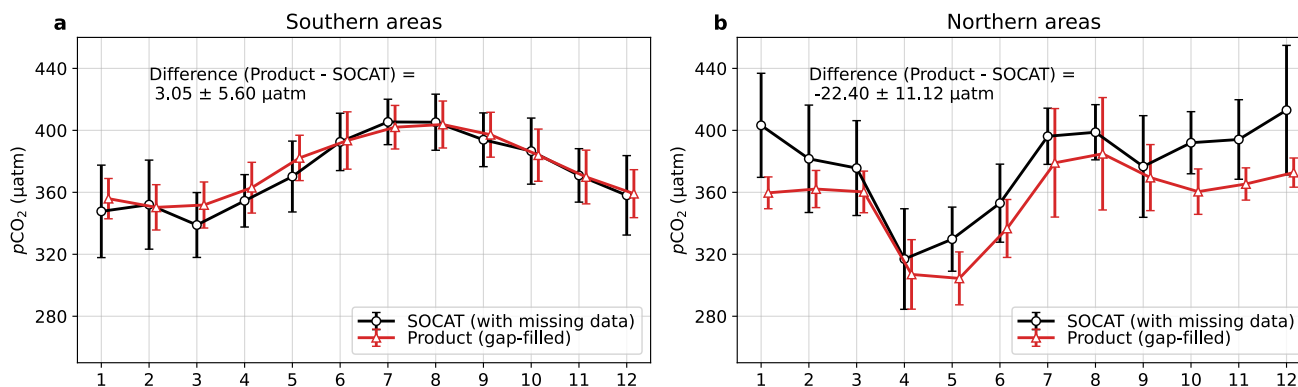
Figure 6. Monthly mean climatology of pCO$_2$ in the southern and northern areas of the NAACOM from 1993 to 2021. Sub-regions are **(a)** southern areas, the red box in Fig. 2, and **(b)** northern areas, the blue box in Fig. 2. Two data representations are shown: (1) SOCAT observations (black curves), which may be influenced by missing data; and (2) the complete gap-filled product output (red curves). Error bars denote one standard deviation of the monthly mean climatology of pCO$_2$. Numbers indicate the mean difference (± one standard deviation) between monthly climatological pCO$_2$ calculated from the two sources, with positive values indicating higher product estimates compared to SOCAT observations. The x-axis shows months (1-12, where 1 represents January), and the y-axis shows pCO$_2$ in µatm.

One of the primary objectives of this product is to capture the seasonal cycle of pCO$_2$ across the NAACOM region. **Figure 6** showcases the applicability of the product in capturing the pCO$_2$ seasonal cycles across the southern and northern areas of NAACOM (red and blue boxes in **Fig. 2**). The comparison of monthly climatologies between the gap-filled product and

16

SOCAT observations reveals strong agreement in the southern regions, despite of the coverage difference, with product-estimated monthly means being only 3.05 ± 5.60 µatm higher than SOCAT (**Fig. 6a**), suggesting that our product effectively captures the seasonal cycle where data are abundant.

In the northern regions where SOCAT data are sparse, the gap-filling ability of the product is also well demonstrated. In the northern region, the area-average monthly pCO_2 climatology calculated from the continuous reconstructed product are 22 ± 11.12 µatm lower than SOCAT observations, which can be attributed to limited observational coverage in this area. This area is characterized by sparse sampling, with observation density approximately 50% lower than in the southern regions (**Fig. 2**) due to the smaller area and limited cruise coverage. For instance, the GStL region only has one summer cruise in SOCAT database (**Fig. 2b**), and the SS and GoMe have particularly sparse winter observations (**Fig. 2d**). The higher latitudes typically exhibit larger seasonal amplitudes in pCO_2, making the limited sampling from SOCAT particularly problematic for accurate characterization. Our gap-free product provides comprehensive spatial and temporal coverage, enabling more robust analysis of pCO_2 patterns and variability in these historically under-sampled regions.

Over the 29 years period, the product predicts smaller monthly standard deviations in southern regions (less than 40 µatm, error bars in **Fig. 6a**), suggesting higher model accuracy and less interannual variability in these areas. Conversely, larger monthly standard deviations are observed in the northern areas, suggesting potential less accuracy and remarkable interannual variability. However, the larger interannual variability in these areas may be an artifact due to the limited observational data available for regression model training, resulting in greater uncertainty in the predictions. Despite differences in the mean monthly climatology, the similar seasonal pCO_2 cycles calculated from SOCAT and reconstructed product demonstrate the capability of the ReCAD-NAACOM-pCO_2 product to represent seasonal pCO_2 variability across diverse coastal environments. Nevertheless, there exist larger differences between the observations and reconstructed pCO_2 in some months and regions (**Fig. 6b**), highlighting the importance of the gap-free product in an unbiased understanding of regional carbon cycles (Ren et al., 2024). Detailed sea surface pCO_2 seasonal cycles and their controlling mechanism across different sub-regions of the NAACOM will be presented in our subsequent work.

3.4 Evaluating the ability of the products in capturing regional variation by comparing it to global products

The ReCAD-NAACOM-pCO_2 product demonstrates the capability to resolve fine-scale regional spatial distributions of pCO_2. **Figure 7** illustrates the spatial distribution of annual mean climatology of pCO_2 across the NAACOM as observed by SOCAT and predicted by different global open and coastal pCO_2 products. Despite being affected by missing data, SOCAT observations (**Fig. 7a**) reveal significant regional variations in pCO_2. In the Louisiana Shelf (LAS) estuary plume region (box 1 in **Fig. 7**), pCO_2 values consistently remain below 340 µatm, while the West Florida Shelf (WFS, box 2 in **Fig. 7**) exhibits

17

370   elevated values exceeding 400 µatm. These contrasting patterns have been reported in previous regional studies (Kealoha et al., 2020; Robbins et al., 2018; Wu et al., 2024b).
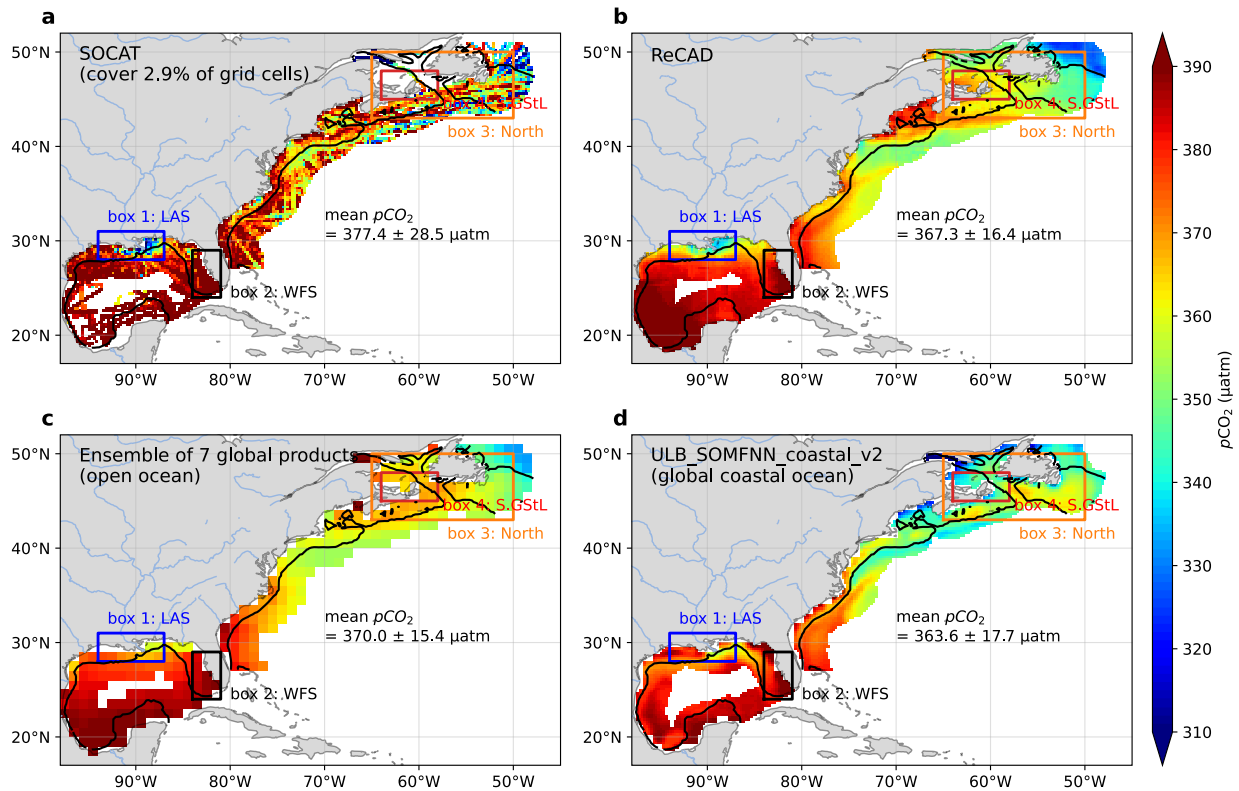
Figure 7. Spatial distribution of annual mean pCO_2 climatology in the NAACOM from different sources. (a) SOCAT observations, **(b)** ReCAD-NAACOM-pCO_2 product, **(c)** Ensemble mean of 7 global open ocean pCO_2 products listed in Table
375   1, and **(d)** Coastal **pCO_2 product** ULB_SOMFFN_coastal_v2 (Roobaert et al., 2024a). The black contour delineates the coastal ocean margin. Three boxes represent sub-regions in the NAACOM: box 1 for the Louisiana Shelf (LAS), box 2 for the West Florida Shelf (WFS), box 3 for the entire Northern region, and box 4 for the southern GStL. (S.GStL). Mean pCO_2 ± standard deviation of all grid cells are provided for each dataset. Color scale represents pCO_2 in µatm.

The ReCAD-NAACOM-pCO_2 product demonstrates superior alignment with SOCAT observations in capturing these regional
380   features that have been reported in previous observation-based studies (**Fig. 7b**), accurately representing the low pCO_2 values in the LAS Mississippi River plume (box 1) and the elevated pCO_2 levels in the WFS (box 2). In contrast, the global reconstructions of pCO_2, represented by the ensemble of the seven open ocean pCO_2 products (**Fig. 7c**), face challenges in resolving these regional pCO_2 variations, as previously discussed in Wu et al (2024b). The coastal pCO_2 product from Roobaert

et al. (2024a, ULB_SOMFFN_coastal_v2) also captures some small-scale structures, like low pCO_2 in the LAS **(Fig. 7d),** but

385 the ReCAD-NAACOM-pCO_2 product exhibits closer values to the observations. In the northern area (box 3), the ReCAD-NAACOM-pCO_2 product predicts higher pCO_2 levels that are closer to observations in the nearshore region (**Fig. 7b**). This is not surprising, as the ULB_SOMFNN_coastal_v2 is a global product known for its high accuracy on the global average.

In addition to these previously documented regional variations, our product reveals several notable features not previously captured by observations or other existing products. For instance, the GoMe displays intermediate pCO_2 levels around 380

390 µatm, distinctly higher than surrounding waters at comparable latitudes, a feature previously documented by a multiple linear regression reconstructed pCO_2 product (Signorini et al., 2013) and five-year (2004-2009) mooring and cruise data (Vandemark et al., 2011) but contradict to another two studies based on numerical models (Cahill et al., 2016; Rutherford et al., 2021). In the southern GStL (S.GStL, box 4 in **Fig. 7**), pCO_2 values are slightly higher compared to adjacent waters at similar latitudes, aligning with high nutrient concentrations typically observed in these river-influenced waters (Lavoie et al., 2021). These

395 regional patterns could not be completely captured by the global products (**Fig. 7c and 7d**). Ability of the ReCAD-NAACOM-pCO_2 product in resolving such regional features demonstrates its potential value for investigating coastal carbon dynamics and their responses to local and regional forcing factors in the NAACOM.

3.5 Evaluating the capacity of the product in detecting decadal linear trends of pCO_2

Using pCO_2 products to accurately reconstruct pCO_2 linear trends in coastal regions presents significant challenges due to the

400 high spatial heterogeneity of coastal pCO_2 dynamics. This heterogeneity often leads to sea surface pCO_2 changes that deviate from atmospheric trends (Laruelle et al., 2018). Even when utilizing similar observational datasets, derived products may not consistently reflect the underlying trends. For instance, Wu et al. (2024b) examined the capability of various products to reflect pCO_2 changes in the GoMx, a region where pCO_2 trends exhibit significant spatial variability. Despite this heterogeneity, seven global open ocean products (listed in **Table 1**) indicate trends similar to atmospheric pCO_2 across the entire GoMx

405 without regional differences. In contrast, the GoMx-specific regional product developed by Chen and Hu (2019) demonstrates no significant overall trend. The discrepancy in trend detection primarily stems from the design of the regression model and the selection of input variables. These factors are critical in capturing the complex spatiotemporal variability of coastal pCO_2 and its long-term evolution.

To assess capability of the product in resolving decadal pCO_2 trends, we conducted an analysis of pCO_2 evolution using three

410 distinct regions within the NAACOM (three boxes in **Fig. 7**) as representative examples (**Fig. 8**). Decadal trends of deseasonalized time series were calculated following the established protocol described by Sutton et al. (2022). The LAS (box 1 in **Fig. 7**) has been identified as an increasing CO_2 sink, characterized by a negative pCO_2 rate increase from 2002-2021 (Wu

et al., 2024). Our product results for the extended period of 1993-2021 indicate that pCO_2 increased at a rate of $+0.44 \pm 0.11$ µatm yr^{-1} (**Fig. 8a**). This rate is significantly lower than the observed atmospheric pCO_2 increase in this region during 2002-

415   2021, which is approximately $+1.8$ µatm yr^{-1}. These findings corroborate our previous conclusion that the LAS is an increasing CO_2 sink, demonstrating the capability our product in revealing long-term pCO_2 trends in this dynamic river plume region, extending the analysis period by nearly a decade compared to previous studies. In contrast, the WFS (box 2 in **Fig. 7**) exhibits accelerated pCO_2 increase faster than atmospheric pCO_2 of around $+2.0$ µatm yr^{-1} (**Fig. 8b**), aligning with observations reported by Robbins et al. (2018), which found a transition from a CO_2 sink to a source in this region during the 1990s.

420   Both ReCAD-NAACOM-pCO_2 and SOCAT consistently report a pCO_2 trend around $+2.3$ to $+2.5$ µatm yr^{-1} in the northern area (box 3 in **Fig. 7**) over 1993-2021 (**Fig. 8c**), which is faster than the atmospheric pCO_2 increase (around $+2.0$ µatm yr^{-1}), suggesting that these areas have been becoming a decreasing CO_2 sink. However, limited observational data in this area necessitates cautious interpretation and warrants further validation in future research. Overall, the spatiotemporal heterogeneity in surface ocean pCO_2 trends across the NAACOM underscores the importance of long-term monitoring to elucidate the drivers

425   of these trends, particularly in regions influenced by major current systems and in areas with limited observational data.
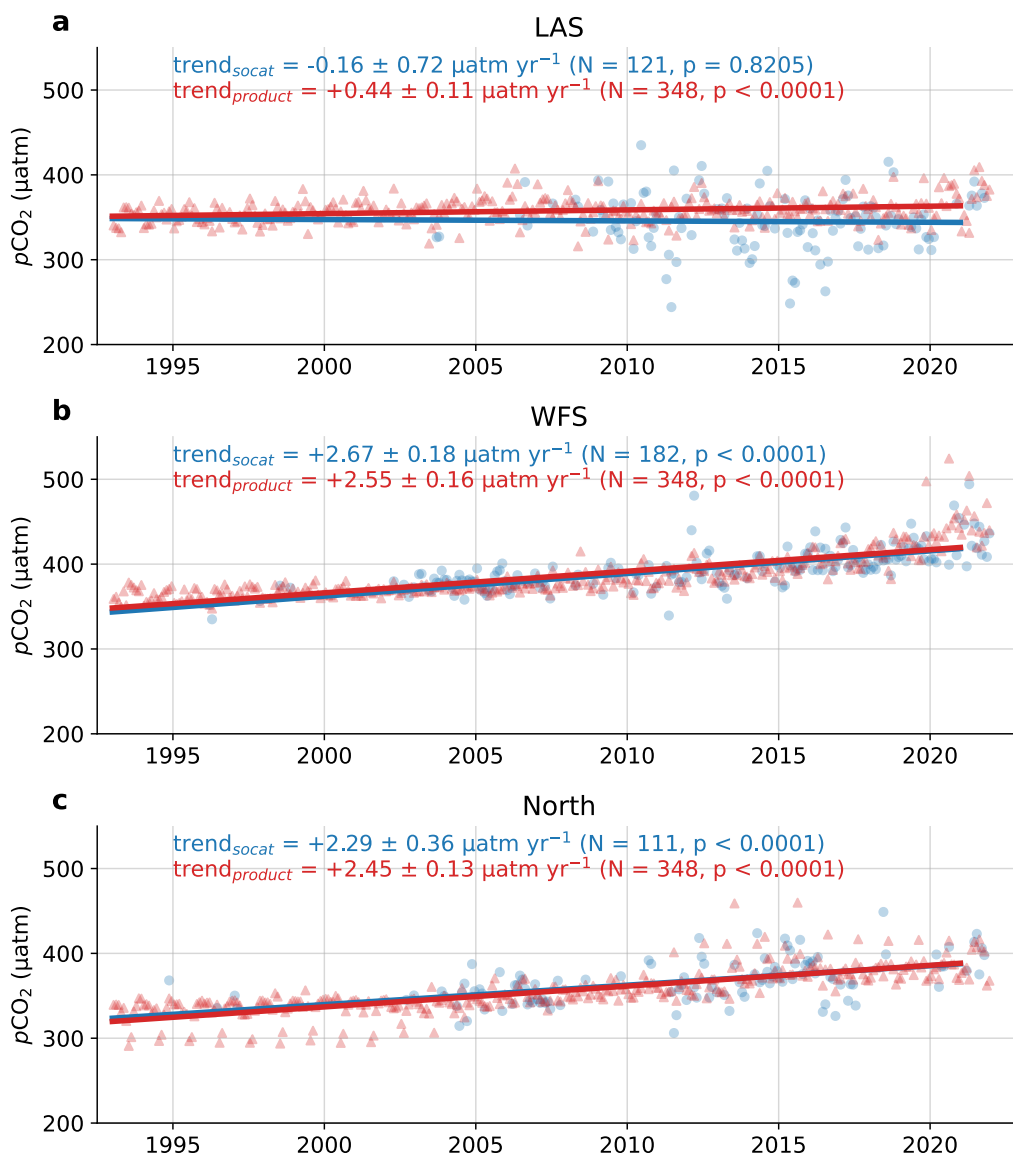
Figure 8. Decadal linear trends of sea surface pCO_2 in three regions of the NAACOM from 1993-2021. Blue and red dots are monthly average pCO_2 values (deseasonalized) calculated from SOCAT observations and reconstructed ReCAD-NAACOM-pCO_2, respectively. Thick lines are linear fitted regression lines. Three regions are the boxes in Fig 7: **(a)** Louisiana Shelf (LAS), northern Gulf of Mexico shelf river plume region; **(b)** West Florida Shelf (WFS); and **(c)** Northern areas. Linear trends are calculated following the established protocol by Sutton et al. (2022). Numbers in parentheses are the number of months with data and the p values.

3.6 Evaluating the uncertainty of the product

Table 3. Uncertainty estimates for the ReCAD-NAACOM-pCO₂ product across different sub-regions of the NAACOM.
u_{obs}, u_{grid}, u_{map}, and u_{inputs} represent the measurement uncertainty, gridding uncertainty, mapping uncertainty, and uncertainty accumulated from input variables, respectively (see method Section 2.5 for further details). u_{pCO_2} is the total combined uncertainty. All values are in µatm. Sub-regions are the Gulf of Mexico (GoMx), South Atlantic Bight (SAB), Mid-Atlantic Bight (MAB), Gulf of Maine (GoMe), Scotian Shelf (SS), and Gulf of St. Lawrence and Grand Banks (GStL&GB).

Region	u_{obs}	u_{grid}	u_{map}	u_{inputs}	u_{pCO_2}
GStL&GB	5.00	15.44	13.57	5.57	21.88
SS	5.00	15.37	13.27	6.18	21.80
GoMe	5.00	16.05	20.12	7.51	27.27
MAB	5.00	16.14	19.49	5.97	26.48
SAB	5.00	8.29	12.03	5.99	16.57
GoMx	5.00	10.38	19.08	5.55	22.97
NAACOM	5.00	12.69	17.89	5.86	23.25

Uncertainty of the reconstructed pCO₂ values in each grid cell was estimated by accumulating uncertainties from mapping (u_{map}), gridding (u_{grid}), measurement (u_{obs}), and input variables (u_{inputs}, see Section 2.5 of the method for further details on the calculation). To maintain a conservative estimate, we adopted the larger value of 5 µatm as u_{obs} for all data points. The gridded fCO₂ values from SOCAT are reported as the averages of all samples collected within each grid cell. Accordingly, u_{grid} was quantified as the standard deviation of samples within each grid cell, calculated across six sub-regions. Following previous literature (Roobaert et al., 2024a; Sharp et al., 2022), u_{map} was calculated using the RMSE values of the model validation phase reported in Table 2. The uncertainty from the validation set (20% of X1) was chosen for its larger sample size than independent test set (X2) and consistency with 10-fold cross-validation results, while avoiding potential underestimation from the training set. u_{inputs} was calculated using a Monte Carlo simulation (**Appendix B**). These four sources of uncertainties were evaluated across different sub-regions of the NAACOM, as shown in **Table 3**. u_{map} contributes the largest portion to the total uncertainties across all sub-subregions with the maximum value up to 20.12 µatm in the GoMe. Overall, the ReCAD-NAACOM-pCO₂ product demonstrates uncertainties ranging between 16 to 28 µatm across six sub-regions, and an average uncertainty of 23.25 µatm for the entire NAACOM.

Our uncertainty estimation employs a conservative estimation, using maximum values at calculation step. This approach likely overestimates the true uncertainty. Despite this conservative method, our calculated uncertainty for the Atlantic margins is comparable to the 43.4 µatm reported by Sharp et al. (2022) for areas within 100 km of the North American Pacific margins. suggesting a good product performance of our product. It is important to note that our uncertainty calculation assumed independence among all sources, which is a simplification. Recent research by Ford et al. (2024) has highlighted that these uncertainties are often correlated. Future studies should consider these inter-variable correlations to refine uncertainty estimates. In addition, the uncertainties reported in this section and provided in the NetCDF file represent the propagated errors

for individual $p\mathrm{CO_2}$ values in each grid cell. Methods to calculate uncertainties in regional averages of $p\mathrm{CO_2}$ or air-sea $\mathrm{CO_2}$ fluxes over specific spatial and temporal domains are detailed in Roobaert et al. (2024) and Landschützer et al. (2014).

3.7 Challenges and limitations

Even though ReCAD-NAACOM-$p\mathrm{CO_2}$ resolves regional $p\mathrm{CO_2}$ variability with high accuracy in the NAACOM, this product still has room for improvement in the future. Potential areas for improvement include the 0.25° spatial resolution, which is inadequate to resolve sub-mesoscale variability at the scale of 0.1 - 10 km (McWilliams, 1985). Furthermore, during the independent validation phase, the accuracy of the model predicted values reduced in the GoMe ($R^2 = 0.49$) and GoMx ($R^2 = 0.46$) **(Table 2)**, which may be due to the complex biological and physical condition in the estuary plume regions in these two gulfs. In this study, we opted not to include chlorophyll-a (Chl-a) concentrations and wind speeds as input variables for model training and prediction. This decision was primarily due to the limited temporal coverage of satellite-derived Chl-a data, which only extends back to 1997 with the launch of the Sea-viewing Wide Field-of-view Sensor (SeaWiFS) satellite (O'Reilly et al., 1998). The inclusion of Chl-a would have restricted the temporal range of our model, potentially limiting its ability to capture long-term trends and variability in $p\mathrm{CO_2}$. Future versions of our model will aim to address this limitation. One potential approach is to develop a two-phase model: one for the period before 1997 without Chl-a data, and another for the post-1997 period incorporating Chl-a information. Alternatively, we may explore methods to reconstruct historical Chl-a data or use proxy variables that correlate with biological productivity and are available for the entire study period.

In our previous work, we demonstrated that incorporating wind speeds and sea surface roughness data derived from Synthetic Aperture Radar (SAR) could enhance model performance in predicting $p\mathrm{CO_2}$ at submesoscale resolutions (Wang et al., 2024). In this work, we evaluated the inclusion of wind speed as an input variable in our model. However, at the 0.25° resolution employed here, the addition of wind speed data did not significantly improve model performance (only increase the R^2 by 0.1). Moreover, using the same Monte Carlo simulation approach applied to other variables, incorporating wind speeds would introduce an additional 6 µatm uncertainty to $p\mathrm{CO_2}$ estimates, doubling the input-related uncertainties. Consequently, we excluded wind speeds from our regression model to reduce input-related uncertainties. Despite this omission, our product demonstrates robust capability in resolving regional variations, seasonal cycles, and decadal trends in $p\mathrm{CO_2}$, making it valuable for future studies.

4 Data availability

The reconstructed $f\mathrm{CO_2}$, $p\mathrm{CO_2}$, and the uncertainty in ReCAD are available as a NetCDF file at https://doi.org/10.5281/zenodo.11500974 (Wu et al., 2024a) and will be updated regularly.

5 Code availability

Python and MATLAB code used to process data and create figures included in this paper is provided at https://github.com/zelunwu/ReCAD_product_v1

490   **6 Conclusions**

The ReCAD-NAACOM-pCO$_2$ product developed in this study represents a significant advancement in our ability to detect the spatial variations, seasonal cycle, and decadal changes of surface ocean pCO$_2$ dynamics in the NAACOM. By leveraging a two-step approach combining random forest and linear regression, and a set of environmental predictors, we have created a high-resolution, long-term dataset (1993-2021 period) that captures the complex spatial and temporal variability of pCO$_2$

495   across the region. On average, compared with all available samples from the SOCAT observations in our study region, the product has an R^2 of 0.92, an RMSE of 12.70 µatm, an MAE of 7.55 µatm, and an MBE of 0.13 µatm for the entire NAACOM, with an average uncertainty of 23.25 µatm. Key findings from this study include:

1. The product demonstrates high accuracy and reliability, as evidenced by strong performance metrics during training, validation, and independent test phases across six sub-regions.

500   2. Distinct seasonal cycles are observed between southern and northern sub-regions, with the product capturing nuanced features such as elevated pCO$_2$ levels during fall and winter in northern areas.

3. Comparison with global products highlights the superior ability of the ReCAD-NAACOM-pCO$_2$ product to resolve fine-scale coastal features and variability.

4. The pCO$_2$ product successfully reconstructed decadal linear trends consistent with previous studies, while also

505   revealing a rapid increase in pCO$_2$ in the northern regions of the NAACOM.

While areas for future improvement exist, such as increasing spatial resolution and enhancing accuracy in estuary plume-influenced regions, the ReCAD-NAACOM-pCO$_2$ product provides a robust foundation for studying coastal carbon dynamics. This dataset will be valuable for investigating air-sea CO$_2$ fluxes, assessing ocean acidification impacts, and understanding the role of coastal systems in the NAACOM.

510   Future research should validate the reconstructed trends, particularly in areas with limited observational data, and explore the mechanisms driving the spatiotemporal variability in pCO$_2$ across the NAACOM region. Additionally, the methodologies developed here can contribute to a more comprehensive understanding of coastal ocean carbon dynamics in the face of climate change and have the potential to be applied globally.

24
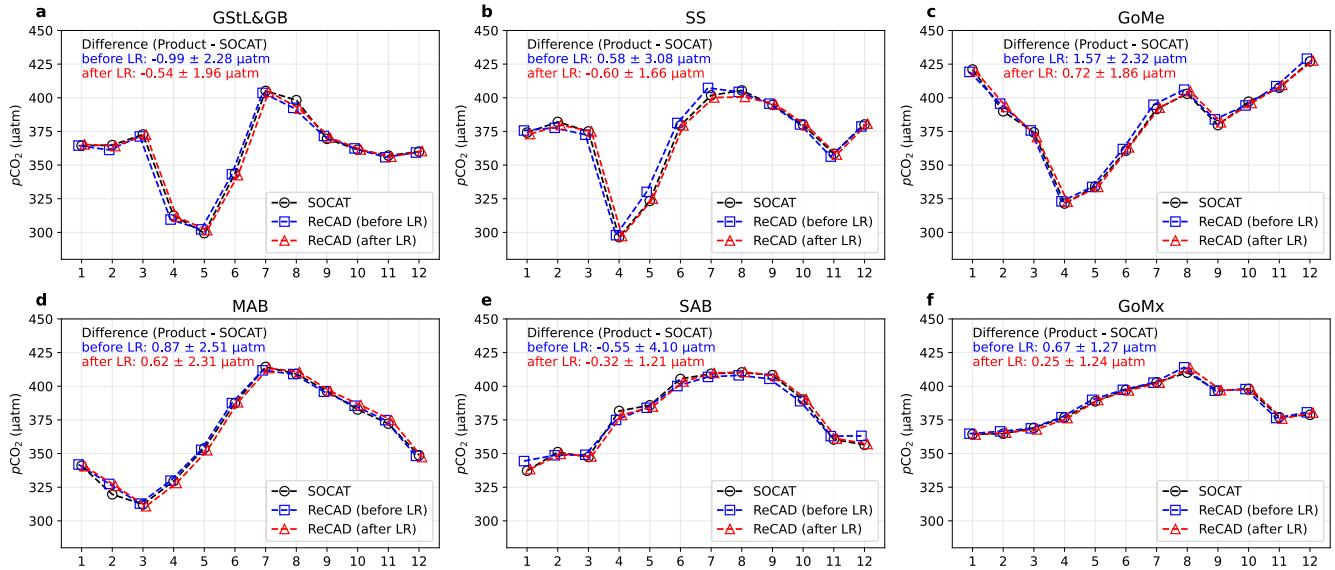
515

Figure A1. Comparisons of monthly pCO$_2$ climatology with SOCAT observations across six sub-regions: evaluations before and after Linear Regression (LR) calibration Values indicate the mean difference (± one standard deviation, blue: before LR, red: after LR) between model-estimated pCO$_2$ and SOCAT observations over the 12-month period, computed only at grid points and times where SOCAT measurements are available.
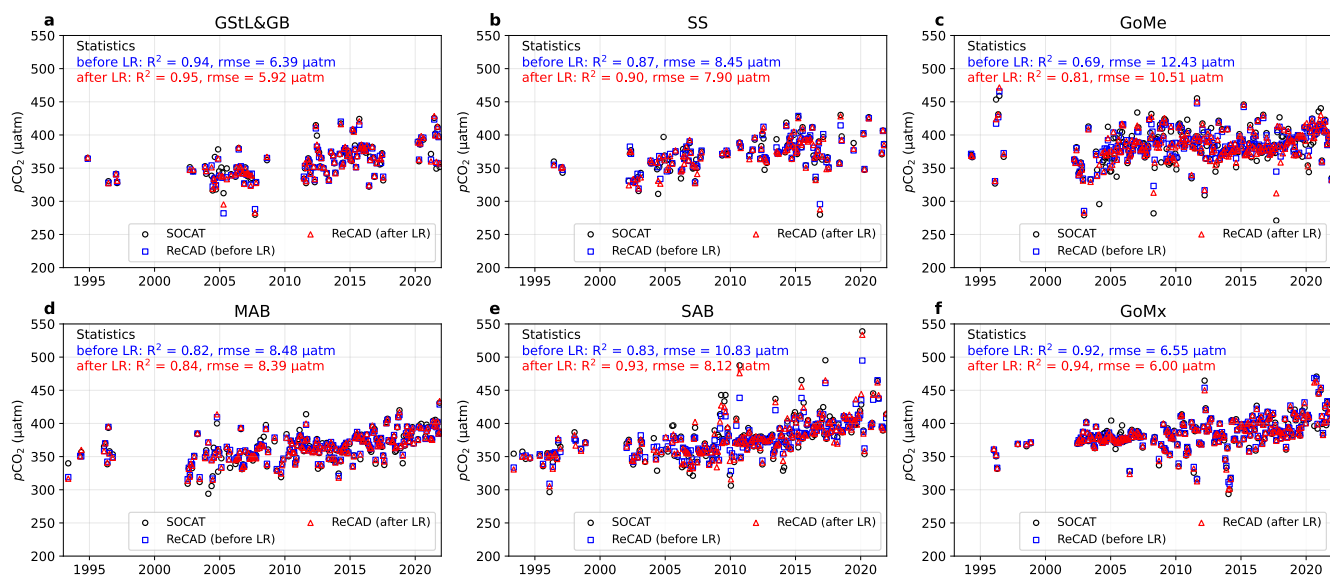
Figure A2. Comparisons of deseasonalized monthly pCO_2 anomalies with SOCAT observations across six sub-regions: evaluations before and after Linear Regression (LR) calibration. Values represent R^2 and RMSE between model-estimated pCO_2 and SOCAT observations (blue: before LR; red: after LR), computed only at grid points and times where SOCAT measurements are available.

Appendix B: Monte Carlo simulation in calculating u_{inputs}

A crucial step in calculating u_{inputs} is determining the uncertainties of the input variables. In our reconstructed model, there were four variables that need to be evaluated: SST, SSS, SSH, and pCO_{2air}. Our general principle was to adopt conservative estimates, using the largest reported uncertainty for each product when available.

SST errors are provided within the OISST product at the grid level. On the global average, OISST reports a mean bias and RMSE of -0.04 and 0.24 ℃ when compared with the observations on the global average (Huang et al., 2021). For our study region, we calculated the mean SST error across all grid cells, yielding a value of 0.23°C.

The SODA database assimilates observational data but does not directly provide SSS error estimates. Given this limitation in uncertainty reporting, we derived an estimate based on the RMSE between model SSS and observations near our study region, as reported by Carton et al. (2018). Their analysis (their Fig. 8) indicates an RMSE exceeding 0.3 psu in the vicinity of our

535   area of interest. In addition, interpolating the 0.5° SSS data to 0.25° resolution could potentially introduce more errors. To maintain a conservative approach in our uncertainty quantification, we doubled the uncertainty and adopted a value of 0.6 psu as the SSS uncertainty for our calculations.

SSH errors are directly provided in the dataset, which has a mean uncertainty of 1.8 cm in our study region.

pCO$_{2air}$, calculated from xCO$_{2air}$ (MBL References), which has a global mean uncertainty of 0.22 ppm.

540   To propagate these input uncertainties to the final pCO$_2$ estimate, a Monte Carlo simulation approach was implemented:

1. For each input variable x_i, random perturbations ε_i were generated following a normal distribution N(0, u_i), where u_i represents the uncertainty of the respective variable listed above.
2. Perturbed inputs ($x_i + \varepsilon_i$) were used to calculate pCO$_2$ using the established model.
3. The difference (Δ_i) between the reconstructed pCO$_2$ before and after adding the perturbation was computed.
545   4. Steps 1, 2, and 3 were iterated 100 times for each input variable.
5. The uncertainty contribution from each variable was quantified as the standard deviation of the 100 Δ_i values in each grid cell.

The total uncertainty attributed to input variables (u_{inputs}) was then calculated as the square root of the quadratic sum of individual uncertainties:

550     $$u_{inputs} = \sqrt{u_{SST}^2 + u_{SSS}^2 + u_{SSH}^2 + u_{pCO_{2air}}^2} \qquad\qquad\qquad\qquad\text{(A1)}$$
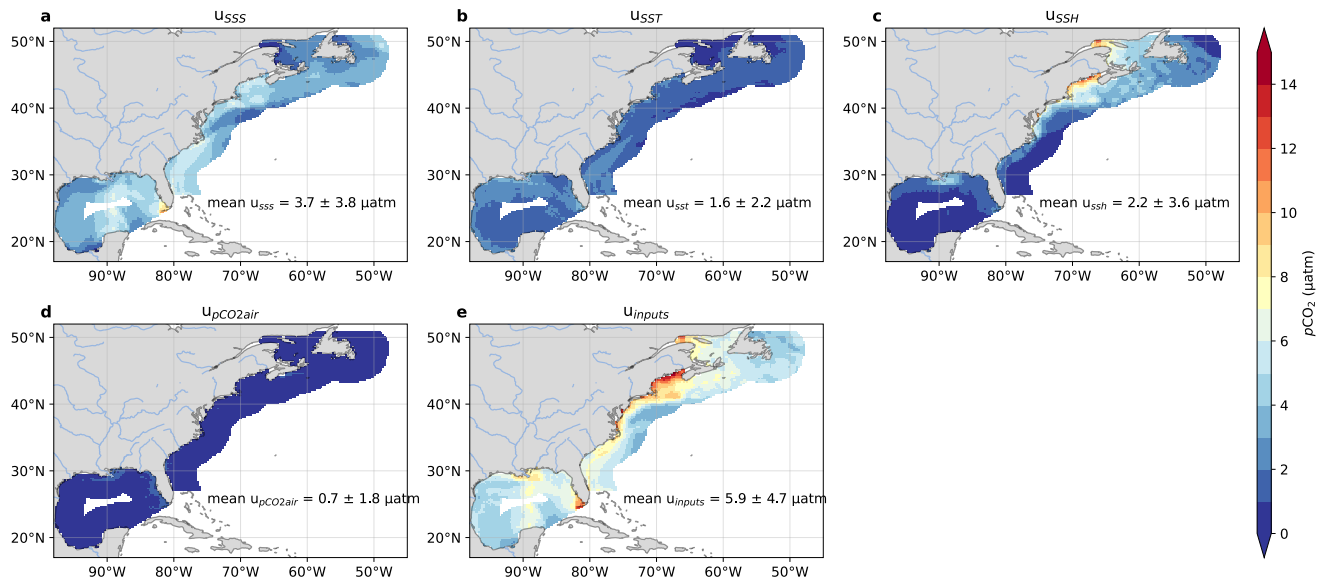
Figure B1. Uncertainties of pCO$_2$ accumulated from different input variables for the model.

The largest uncertainties propagated from these variables are sourced from SSS and SSH **(Fig. A1a and A1c).** Simulating salinity in coastal regions is still challenging due to complex lang-ocean interaction. For the SSH, the largest uncertainties were observed in the GoMe and GStL. Overall, u_{inputs} is largest in the West Florida Shelf and nearshore waters around the GoMe, with a mean u_{inputs} uncertainty of 5.9 ± 4.7 µatm for the entire NAACOM.

555

Author contribution

Zelun Wu: Conceptualization, data curation, formal analysis, methodology, software, visualization, writing – original draft preparation, writing – review & editing. **Wenfang Lu**: Funding acquisition, methodology, validation, writing – review & editing. **Alizée Roobaert**: Validation, writing – review & editing. **Luping Song**: Validation, writing – review & editing. **Xiao-Hai Yan**: Project administration, supervision. **Wei-Jun Cai**: Conceptualization, project administration, supervision, validation, writing – review & editing.

Competing interests

The authors declare that they have no conflict of interest.

Disclaimer

Special issue statement

Acknowledgments

References

Bakker, D. C. E., Pfeil, B., Landa, C. S., Metzl, N., O'Brien, K. M., Olsen, A., Smith, K., Cosca, C., Harasawa, S., Jones, S.
585 D., Nakaoka, S., Nojiri, Y., Schuster, U., Steinhoff, T., Sweeney, C., Takahashi, T., Tilbrook, B., Wada, C., Wanninkhof, R., Alin, S. R., Balestrini, C. F., Barbero, L., Bates, N. R., Bianchi, A. A., Bonou, F., Boutin, J., Bozec, Y., Burger, E. F., Cai, W.-J., Castle, R. D., Chen, L., Chierici, M., Currie, K., Evans, W., Featherstone, C., Feely, R. A., Fransson, A., Goyet, C., Greenwood, N., Gregor, L., Hankin, S., Hardman-Mountford, N. J., Harlay, J., Hauck, J., Hoppema, M., Humphreys, M. P., Hunt, C. W., Huss, B., Ibánhez, J. S. P., Johannessen, T., Keeling, R., Kitidis, V., Körtzinger, A., Kozyr, A., Krasakopoulou,
590 E., Kuwata, A., Landschützer, P., Lauvset, S. K., Lefèvre, N., Lo Monaco, C., Manke, A., Mathis, J. T., Merlivat, L., Millero, F. J., Monteiro, P. M. S., Munro, D. R., Murata, A., Newberger, T., Omar, A. M., Ono, T., Paterson, K., Pearce, D., Pierrot, D., Robbins, L. L., Saito, S., Salisbury, J., Schlitzer, R., Schneider, B., Schweitzer, R., Sieger, R., Skjelvan, I., Sullivan, K. F., Sutherland, S. C., Sutton, A. J., Tadokoro, K., Telszewski, M., Tuma, M., van Heuven, S. M. A. C., Vandemark, D., Ward, B., Watson, A. J., and Xu, S.: A multi-decade record of high-quality CO_2 data in version 3 of the Surface Ocean CO_2 Atlas
595 (SOCAT), Earth Syst. Sci. Data, 8, 383–413, https://doi.org/10.5194/essd-8-383-2016, 2016.

Breiman, L.: Random Forests, Machine Learning, 45, 5–32, https://doi.org/10.1023/A:1010933404324, 2001.

Cahill, B., Wilkin, J., Fennel, K., Vandemark, D., and Friedrichs, M. A. M.: Interannual and seasonal variabilities in air-sea CO_2 fluxes along the U.S. eastern continental shelf and their sensitivity to increasing air temperatures and variable winds: U.S. East Coast Shelf Air-Sea CO_2 Fluxes, J. Geophys. Res. Biogeosci., 121, 295–311, https://doi.org/10.1002/2015JG002939,
600 2016.

Cai, W.-J., Xu, Y.-Y., Feely, R. A., Wanninkhof, R., Jönsson, B., Alin, S. R., Barbero, L., Cross, J. N., Azetsu-Scott, K., Fassbender, A. J., Carter, B. R., Jiang, L.-Q., Pepin, P., Chen, B., Hussain, N., Reimer, J. J., Xue, L., Salisbury, J. E., Hernández-Ayón, J. M., Langdon, C., Li, Q., Sutton, A. J., Chen, C.-T. A., and Gledhill, D. K.: Controls on surface water carbonate chemistry along North American ocean margins, Nat Commun, 11, 2691, https://doi.org/10.1038/s41467-020-
605 16530-z, 2020.

Carter, B. R., Feely, R. A., Williams, N. L., Dickson, A. G., Fong, M. B., and Takeshita, Y.: Updated methods for global locally interpolated estimation of alkalinity, pH, and nitrate: LIR: Global alkalinity, pH, and nitrate estimates, Limnol. Oceanogr. Methods, 16, 119–131, https://doi.org/10.1002/lom3.10232, 2018.

Carton, J. A., Chepurin, G. A., and Chen, L.: SODA3: A New Ocean Climate Reanalysis, J. Climate, 31, 6967–6983,
610 https://doi.org/10.1175/JCLI-D-18-0149.1, 2018.

Chau, T. T. T., Gehlen, M., and Chevallier, F.: A seamless ensemble-based reconstruction of surface ocean pCO_2 and air–sea CO_2 fluxes over the global coastal and open oceans, Biogeosciences, 19, 1087–1109, https://doi.org/10.5194/bg-19-1087-2022, 2022.

Chen, C.-T. A., Huang, T.-H., Chen, Y.-C., Bai, Y., He, X., and Kang, Y.: Air–sea exchanges of CO_2 in the world's coastal
615   seas, Biogeosciences, 10, 6509–6544, https://doi.org/10.5194/bg-10-6509-2013, 2013.

Chen, S. and Hu, C.: Environmental controls of surface water pCO_2 in different coastal environments: Observations from
marine buoys, Continental Shelf Research, 183, 73–86, https://doi.org/10.1016/j.csr.2019.06.007, 2019.

Dai, M., Su, J., Zhao, Y., Hofmann, E. E., Cao, Z., Cai, W.-J., Gan, J., Lacroix, F., Laruelle, G. G., Meng, F., Müller, J. D.,
Regnier, P. A. G., Wang, G., and Wang, Z.: Carbon Fluxes in the Coastal Ocean: Synthesis, Boundary Processes and Future
620   Trends, Annu. Rev. Earth Planet. Sci., 50, annurev-earth-032320-090746, https://doi.org/10.1146/annurev-earth-032320-
090746, 2022.

Dlugokencky, E. and Tans, P.: Trends in atmospheric carbon dioxide, National Oceanic and Atmospheric Administration,
Global Monitoring Laboratory (NOAA/GML), 2022.

European Union-Copernicus Marine Service: GLOBAL OCEAN GRIDDED L4 SEA SURFACE HEIGHTS AND DERIVED
625   VARIABLES REPROCESSED (1993-ONGOING), https://doi.org/10.48670/MOI-00148, 2021.

Fay, A. R., Gregor, L., Landschützer, P., McKinley, G. A., Gruber, N., Gehlen, M., Iida, Y., Laruelle, G. G., Rödenbeck, C.,
Roobaert, A., and Zeng, J.: SeaFlux: harmonization of air–sea CO2 fluxes from surface pCO2 data products using a
standardized approach, Earth Syst. Sci. Data, 13, 4693–4710, https://doi.org/10.5194/essd-13-4693-2021, 2021.

Fennel, K. and Wilkin, J.: Quantifying biological carbon export for the northwest North Atlantic continental shelves,
630   Geophysical Research Letters, 36, https://doi.org/10.1029/2009GL039818, 2009.

Fennel, K., Alin, S., Barbero, L., Evans, W., Bourgeois, T., Cooley, S., Dunne, J., Feely, R. A., Hernandez-Ayon, J. M., Hu,
X., Lohrenz, S., Muller-Karger, F., Najjar, R., Robbins, L., Shadwick, E., Siedlecki, S., Steiner, N., Sutton, A., Turk, D.,
Vlahos, P., and Wang, Z. A.: Carbon cycling in the North American coastal ocean: a synthesis, Biogeosciences, 16, 1281–
1304, https://doi.org/10.5194/bg-16-1281-2019, 2019.

635   Ford, D. J., Blannin, J., Watts, J., Watson, A., Landschützer, P., Jersild, A., and Shutler, J.: A comprehensive analysis of air-
sea   CO2   flux   uncertainties   constructed   from   surface   ocean   data   products,
https://doi.org/10.22541/essoar.171199280.05732707/v1, 1 April 2024.

Friedlingstein, P., O'Sullivan, M., Jones, M. W., Andrew, R. M., Bakker, D. C. E., Hauck, J., Landschützer, P., Le Quéré, C.,
Luijkx, I. T., Peters, G. P., Peters, W., Pongratz, J., Schwingshackl, C., Sitch, S., Canadell, J. G., Ciais, P., Jackson, R. B.,
640   Alin, S. R., Anthoni, P., Barbero, L., Bates, N. R., Becker, M., Bellouin, N., Decharme, B., Bopp, L., Brasika, I. B. M., Cadule,
P., Chamberlain, M. A., Chandra, N., Chau, T.-T.-T., Chevallier, F., Chini, L. P., Cronin, M., Dou, X., Enyo, K., Evans, W.,
Falk, S., Feely, R. A., Feng, L., Ford, D. J., Gasser, T., Ghattas, J., Gkritzalis, T., Grassi, G., Gregor, L., Gruber, N., Gürses,
Ö., Harris, I., Hefner, M., Heinke, J., Houghton, R. A., Hurtt, G. C., Iida, Y., Ilyina, T., Jacobson, A. R., Jain, A., Jarníková,
T., Jersild, A., Jiang, F., Jin, Z., Joos, F., Kato, E., Keeling, R. F., Kennedy, D., Klein Goldewijk, K., Knauer, J., Korsbakken,
645   J. I., Körtzinger, A., Lan, X., Lefèvre, N., Li, H., Liu, J., Liu, Z., Ma, L., Marland, G., Mayot, N., McGuire, P. C., McKinley,
G. A., Meyer, G., Morgan, E. J., Munro, D. R., Nakaoka, S.-I., Niwa, Y., O'Brien, K. M., Olsen, A., Omar, A. M., Ono, T.,
Paulsen, M., Pierrot, D., Pocock, K., Poulter, B., Powis, C. M., Rehder, G., Resplandy, L., Robertson, E., Rödenbeck, C.,
Rosan, T. M., Schwinger, J., Séférian, R., et al.: Global Carbon Budget 2023, Earth Syst. Sci. Data, 15, 5301–5369,
https://doi.org/10.5194/essd-15-5301-2023, 2023.

650 Fu, Z., Hu, L., Chen, Z., Zhang, F., Shi, Z., Hu, B., Du, Z., and Liu, R.: Estimating spatial and temporal variation in ocean surface pCO2 in the Gulf of Mexico using remote sensing and machine learning techniques, Science of The Total Environment, 745, 140965, https://doi.org/10.1016/j.scitotenv.2020.140965, 2020.

Gloege, L., Yan, M., Zheng, T., and McKinley, G. A.: Improved Quantification of Ocean Carbon Uptake by Using Machine Learning to Merge Global Models and pCO $_2$ Data, J Adv Model Earth Syst, 14, https://doi.org/10.1029/2021MS002620, 2022.

655 Gregor, L. and Gruber, N.: OceanSODA-ETHZ: A global gridded data set of the surface ocean carbonate system for seasonal to decadal studies of ocean acidification, Earth System Science Data, 13, 777–808, https://doi.org/10.5194/essd-13-777-2021, 2021.

Hersbach, H., Bell, B., Berrisford, P., Biavati, G., Horányi, A., Muñoz Sabater, J., Nicolas, J., Peubey, C., Radu, R., Rozum, I., and others: ERA5 monthly averaged data on single levels from 1979 to present, Copernicus Climate Change Service (C3S)
660 Climate Data Store (CDS), 10, 252–266, https://doi.org/10.24381/cds.f17050d7, 2019.

Huang, B., Liu, C., Banzon, V., Freeman, E., Graham, G., Hankins, B., Smith, T., and Zhang, H.-M.: Improvements of the Daily Optimum Interpolation Sea Surface Temperature (DOISST) Version 2.1, Journal of Climate, 34, 2923–2939, https://doi.org/10.1175/JCLI-D-20-0166.1, 2021.

Hughes, I. and Hase, T. P. A.: Measurements and their uncertainties: a practical guide to modern error analysis, New York : 665 Oxford University Press, Oxford, 136 pp., 2010.

Iida, Y., Takatani, Y., Kojima, A., and Ishii, M.: Global trends of ocean CO2 sink and ocean acidification: an observation-based reconstruction of surface ocean inorganic carbon variables, J Oceanogr, 77, 323–358, https://doi.org/10.1007/s10872-020-00571-5, 2021.

Kealoha, A. K., Shamberger, K. E. F., DiMarco, S. F., Thyng, K. M., Hetland, R. D., Manzello, D. P., Slowey, N. C., and
670 Enochs, I. C.: Surface Water CO $_2$ variability in the Gulf of Mexico (1996–2017), Sci Rep, 10, 12279, https://doi.org/10.1038/s41598-020-68924-0, 2020.

Landschützer, P., Gruber, N., Bakker, D. C. E., and Schuster, U.: Recent variability of the global ocean carbon sink, Global Biogeochemical Cycles, 28, 927–949, https://doi.org/10.1002/2014GB004853, 2014.

Landschützer, P., Gruber, N., and Bakker, D. C. E.: An observation-based global monthly gridded sea surface pCO2 product
675 from 1982 onward and its monthly climatology (NCEI Accession 0160558), https://doi.org/10.7289/V5Z899N6, 2017.

Landschützer, P., Laruelle, G. G., Roobaert, A., and Regnier, P.: A uniform pCO $_2$ climatology combining open and coastal oceans, Earth Syst. Sci. Data, 12, 2537–2553, https://doi.org/10.5194/essd-12-2537-2020, 2020.

Laruelle, G. G., Landschützer, P., Gruber, N., Tison, J.-L., Delille, B., and Regnier, P.: Global high-resolution monthly pCO $_2$ climatology for the coastal ocean derived from neural network interpolation, Biogeosciences, 14, 4545–4561,
680 https://doi.org/10.5194/bg-14-4545-2017, 2017.

Laruelle, G. G., Cai, W.-J., Hu, X., Gruber, N., Mackenzie, F. T., and Regnier, P.: Continental shelves as a variable but increasing global sink for atmospheric carbon dioxide, Nat Commun, 9, 454, https://doi.org/10.1038/s41467-017-02738-z, 2018.

Lavoie, D., Lambert, N., Starr, M., Chassé, J., Riche, O., Le Clainche, Y., Azetsu-Scott, K., Béjaoui, B., Christian, J. R., and Gilbert, D.: The Gulf of St. Lawrence Biogeochemical Model: A Modelling Tool for Fisheries and Ocean Management, Front. Mar. Sci., 8, 732269, https://doi.org/10.3389/fmars.2021.732269, 2021.

Lohrenz, S. E. and Cai, W.-J.: Satellite ocean color assessment of air-sea fluxes of CO_2 in a river-dominated coastal margin: CO_2 FLUXES IN A RIVER-DOMINATED MARGIN, Geophys. Res. Lett., 33, https://doi.org/10.1029/2005GL023942, 2006.

Lu, W., Su, H., Yang, X., and Yan, X.-H.: Subsurface temperature estimation from remote sensing data using a clustering-neural network method, Remote Sensing of Environment, 229, 213–222, https://doi.org/10.1016/j.rse.2019.04.009, 2019.

McWilliams, J. C.: Submesoscale, coherent vortices in the ocean, Reviews of Geophysics, 23, 165–182, https://doi.org/10.1029/RG023i002p00165, 1985.

O'Reilly, J. E., Maritorena, S., Mitchell, B. G., Siegel, D. A., Carder, K. L., Garver, S. A., Kahru, M., and McClain, C.: Ocean color chlorophyll algorithms for SeaWiFS, J. Geophys. Res., 103, 24937–24953, https://doi.org/10.1029/98JC02160, 1998.

Ren, H., Lu, W., Xiao, W., Zhu, Q., Xiao, C., and Lai, Z.: Intraseasonal response of marine planktonic ecosystem to summertime Madden-Julian Oscillation in the South China Sea: A model study, Progress in Oceanography, 224, 103251, https://doi.org/10.1016/j.pocean.2024.103251, 2024.

Robbins, L. L., Daly, K. L., Barbero, L., Wanninkhof, R., He, R., Zong, H., Lisle, J. T., Cai, W. -J., and Smith, C. G.: Spatial and Temporal Variability of $p$$CO_2$, Carbon Fluxes, and Saturation State on the West Florida Shelf, J. Geophys. Res. Oceans, 123, 6174–6188, https://doi.org/10.1029/2018JC014195, 2018.

Rödenbeck, C., DeVries, T., Hauck, J., Le Quéré, C., and Keeling, R. F.: Data-based estimates of interannual sea–air CO2 flux variations 1957–2020 and their relation to environmental drivers, Biogeosciences, 19, 2627–2652, https://doi.org/10.5194/bg-19-2627-2022, 2022.

Roobaert, A., Resplandy, L., Laruelle, G. G., Liao, E., and Regnier, P.: A framework to evaluate and elucidate the driving mechanisms of coastal sea surface $p$$CO_2$ seasonality using an ocean general circulation model (MOM6-COBALT), Ocean Sci., 18, 67–88, https://doi.org/10.5194/os-18-67-2022, 2022.

Roobaert, A., Regnier, P., Landschützer, P., and Laruelle, G. G.: A novel sea surface pCO2-product for the global coastal ocean resolving trends over 1982–2020, Earth Syst. Sci. Data, 16, 421–441, https://doi.org/10.5194/essd-16-421-2024, 2024a.

Roobaert, A., Resplandy, L., Laruelle, G. G., Liao, E., and Regnier, P.: Unraveling the Physical and Biological Controls of the Global Coastal CO_2 Sink, Global Biogeochemical Cycles, 38, e2023GB007799, https://doi.org/10.1029/2023GB007799, 2024b.

Ross, A. C., Stock, C. A., Adcroft, A., Curchitser, E., Hallberg, R., Harrison, M. J., Hedstrom, K., Zadeh, N., Alexander, M., Chen, W., Drenkard, E. J., Du Pontavice, H., Dussin, R., Gomez, F., John, J. G., Kang, D., Lavoie, D., Resplandy, L., Roobaert, A., Saba, V., Shin, S.-I., Siedlecki, S., and Simkins, J.: A high-resolution physical–biogeochemical model for marine resource applications in the northwest Atlantic (MOM6-COBALT-NWA12 v1.0), Geosci. Model Dev., 16, 6943–6985, https://doi.org/10.5194/gmd-16-6943-2023, 2023.

Rutherford, K., Fennel, K., Atamanchuk, D., Wallace, D., and Thomas, H.: A modelling study of temporal and spatial pCO_2 variability on the biologically active and temperature-dominated Scotian Shelf, Biogeosciences, 18, 6271–6286, https://doi.org/10.5194/bg-18-6271-2021, 2021.

Salisbury, J. E. and Jönsson, B. F.: Rapid warming and salinity changes in the Gulf of Maine alter surface ocean carbonate parameters and hide ocean acidification, Biogeochemistry, 141, 401–418, https://doi.org/10.1007/s10533-018-0505-3, 2018.

Sharp, J. D., Fassbender, A. J., Carter, B. R., Lavin, P. D., and Sutton, A. J.: A monthly surface pCO2 product for the California Current Large Marine Ecosystem, Earth Syst. Sci. Data, 14, 2081–2108, https://doi.org/10.5194/essd-14-2081-2022, 2022.

Signorini, S. R., Mannino, A., Najjar, R. G., Friedrichs, M. A. M., Cai, W.-J., Salisbury, J., Wang, Z. A., Thomas, H., and Shadwick, E.: Surface ocean pCO_2 seasonality and sea-air CO_2 flux estimates for the North American east coast, J. Geophys. Res. Oceans, 118, 5439–5460, https://doi.org/10.1002/jgrc.20369, 2013.

Song, L., Lee, Z., Shang, S., Huang, B., Wu, J., Wu, Z., Lu, W., and Liu, X.: On the spatial and temporal variations of primary production in the South China Sea, IEEE Trans. Geosci. Remote Sensing, 1–1, https://doi.org/10.1109/TGRS.2023.3241209, 2023.

Su, H., Zhang, H., Geng, X., Qin, T., Lu, W., and Yan, X.-H.: OPEN: A New Estimation of Global Ocean Heat Content for Upper 2000 Meters from Remote Sensing Data, Remote Sensing, 12, 2294, https://doi.org/10.3390/rs12142294, 2020.

Sutton, A. J., Battisti, R., Carter, B., Evans, W., Newton, J., Alin, S., Bates, N. R., Cai, W.-J., Currie, K., Feely, R. A., Sabine, C., Tanhua, T., Tilbrook, B., and Wanninkhof, R.: Advancing best practices for assessing trends of ocean acidification time series, Front. Mar. Sci., 9, 1045667, https://doi.org/10.3389/fmars.2022.1045667, 2022.

Takahashi, T., Sutherland, S. C., and Kozyr, A.: Global Ocean Surface Water Partial Pressure of CO_2 Database: Measurements Performed During 1957-2018 (LDEO Database Version 2018) (NCEI Accession 0160492), 2019.

Taylor, J. R.: An introduction to error analysis: the study of uncertainties in physical measurements, 2nd ed., University Science Books, Sausalito, Calif, 327 pp., 1997.

Vandemark, D., Salisbury, J. E., Hunt, C. W., Shellito, S. M., Irish, J. D., McGillis, W. R., Sabine, C. L., and Maenner, S. M.: Temporal and spatial dynamics of CO_2 air-sea flux in the Gulf of Maine, J. Geophys. Res., 116, C01012, https://doi.org/10.1029/2010JC006408, 2011.

Wang, T., Yu, P., Wu, Z., Lu, W., Liu, X., Li, Q. P., and Huang, B.: Revisiting the Intraseasonal Variability of Chlorophyll-a in the Adjacent Luzon Strait With a New Gap-Filled Remote Sensing Data Set, IEEE Trans. Geosci. Remote Sensing, 1–11, https://doi.org/10.1109/TGRS.2021.3067646, 2021.

Wang, Y., Wu, Z., Lu, W., Yu, S., Li, S., Meng, L., Geng, X., and Yan, X.-H.: Remote sensing estimations of the seawater partial pressure of CO_2 using sea surface roughness derived from Synthetic Aperture Radar, IEEE Trans. Geosci. Remote Sensing, 1–1, https://doi.org/10.1109/TGRS.2024.3379984, 2024.

Wang, Z., Wang, G., Guo, X., Bai, Y., Xu, Y., and Dai, M.: Spatial reconstruction of long-term (2003–2020) sea surface pCO_2 in the South China Sea using a machine-learning-based regression method aided by empirical orthogonal function analysis, Earth Syst. Sci. Data, 15, 1711–1731, https://doi.org/10.5194/essd-15-1711-2023, 2023.

Wang, Z. A., Bienvenu, D. J., Mann, P. J., Hoering, K. A., Poulsen, J. R., Spencer, R. G. M., and Holmes, R. M.: Inorganic carbon speciation and fluxes in the Congo River: THE CONGO RIVER INORGANIC CARBON SYSTEM, Geophys. Res. Lett., 40, 511–516, https://doi.org/10.1002/grl.50160, 2013.

755 Wanninkhof, R., Barbero, L., Byrne, R., Cai, W.-J., Huang, W.-J., Zhang, J.-Z., Baringer, M., and Langdon, C.: Ocean acidification along the Gulf Coast and East Coast of the USA, Continental Shelf Research, 98, 54–71, https://doi.org/10.1016/j.csr.2015.02.008, 2015.

Weiss, R. F. and Price, B. A.: Nitrous oxide solubility in water and seawater, Marine Chemistry, 8, 347–359, https://doi.org/10.1016/0304-4203(80)90024-9, 1980.

760 Wu, Z., Lu, W., Yan, X.-H., and Cai, W.-J.: A Reconstructed Coastal Acidification Database (ReCAD) pCO2 data product for the North American Atlantic Coastal Ocean Margins, https://doi.org/10.5281/ZENODO.11500974, 2024a.

Wu, Z., Wang, H., Liao, E., Hu, C., Edwing, K., Yan, X.-H., and Cai, W.-J.: Air-sea CO_2 flux in the Gulf of Mexico from observations and multiple machine-learning data products, Progress in Oceanography, 103244, https://doi.org/10.1016/j.pocean.2024.103244, 2024b.

765 Xu, Y., Cai, W., Wanninkhof, R., Salisbury, J., Reimer, J., and Chen, B.: Long-Term Changes of Carbonate Chemistry Variables Along the North American East Coast, J. Geophys. Res. Oceans, 125, https://doi.org/10.1029/2019JC015982, 2020.

Yang, G. G., Wang, Q., Feng, J., He, L., Li, R., Lu, W., Liao, E., and Lai, Z.: Can three-dimensional nitrate structure be reconstructed from surface information with artificial intelligence? — A proof-of-concept study, Science of The Total Environment, 924, 171365, https://doi.org/10.1016/j.scitotenv.2024.171365, 2024.

770 Zeng, J., Nojiri, Y., Landschützer, P., Telszewski, M., and Nakaoka, S.: A Global Surface Ocean fCO2 Climatology Based on a Feed-Forward Neural Network, Journal of Atmospheric and Oceanic Technology, 31, 1838–1849, https://doi.org/10.1175/JTECH-D-13-00137.1, 2014.